Monsoon Mission Coupled Forecast System Version 2.0: Model Description and Indian Monsoon Simulations

Deepeshkumar Jain[1,2], Suryachandra A. Rao[1*], Ramu Dandi[1], Prasanth A. Pillai[1], Ankur Srivastava[1], Maheswar Pradhan[1], Kiran Valappil Gangadharan[1]

[1*]Monsoon Mission, Indian Institute of Tropical Meteorology, Ministry of Earth Sciences, Pashan, Pune, 411008, Maharashtra, India.

[2]NCMRWF, Ministry of Earth Sciences, A50, Noida, 201309, UP, India.

*Corresponding author(s). E-mail(s): surya@tropmet.res.in;

Contributing authors: deepeshkumar@tropmet.res.in; daramu@tropmet.res.in; prasanth@tropmet.res.in; ankur.cat@tropmet.res.in; maheshwar.cat@tropmet.res.in, kiran.v@tropmet.res.in

Abstract. We present the Monsoon Mission Coupled Forecast System version 2 (MMCFSv2) model, which substantially upgrades the present operational MMCFSv1 (version 1) at the India Meteorology Department. The latest 25 years (1998-2022) of retrospective seasonal coupled hindcast simulations of the Indian Summer Monsoon with April initial conditions from Coupled Forecast System Reanalysis are discussed. MMCFSv2 simulates the tropical wind, rainfall, and temperature structure reasonably well. MMCFSv2 captures surface winds well and reduces precipitation biases over land, except over India and North America. The dry bias over these regions remained like MMCFSv1. MMCFSv2 captures significant features of the Indian monsoon, including the intensity and location of the maximum precipitation centres and the large-scale monsoon circulation. MMCFSv2 improves the phase skill (anomaly correlation coefficient) of the interannual variation of ISMR by 17 % and enhances the amplitude skill (Normalized Root Mean Square Error) by 20 %. MMCFSv2 shows improved teleconnections of ISMR with the equatorial Indian and Pacific oceans. This 25-year hindcast dataset will serve as the baseline for future sensitivity studies of MMCFSv2.

1. Introduction

Over a third of the world's population resides in the East Asian and the Indian sub-continent region, most of which depends on the natural irrigation from the summer monsoon rainfall for agricultural production (Gadgil, 2006). Indian summer monsoon (ISM), which lasts from June to September every year, is a perennial system. It, however, shows interannual and intra-seasonal variability (Parthasarthi et al., 1993; Kumar et al., 1999; Munot et al., 2000; Mohan et al., 2000; Gadgil et al., 2003) affecting the region's agricultural production (Gadgil, 2006). A 10 % deviation from the climatological mean is sufficient to have an excess or a deficient monsoon over India (Singh et al., 2015). The standard deviation, variance, and their ratio with mean of June-September (JJAS) mean precipitation (Fig. 1) shows that the location of highest variability is over oceans. In contrast, the variability over the Indian landmass is low despite the high mean precipitation. This low variability (having a high impact on agricultural production) challenges the models trying to predict it.
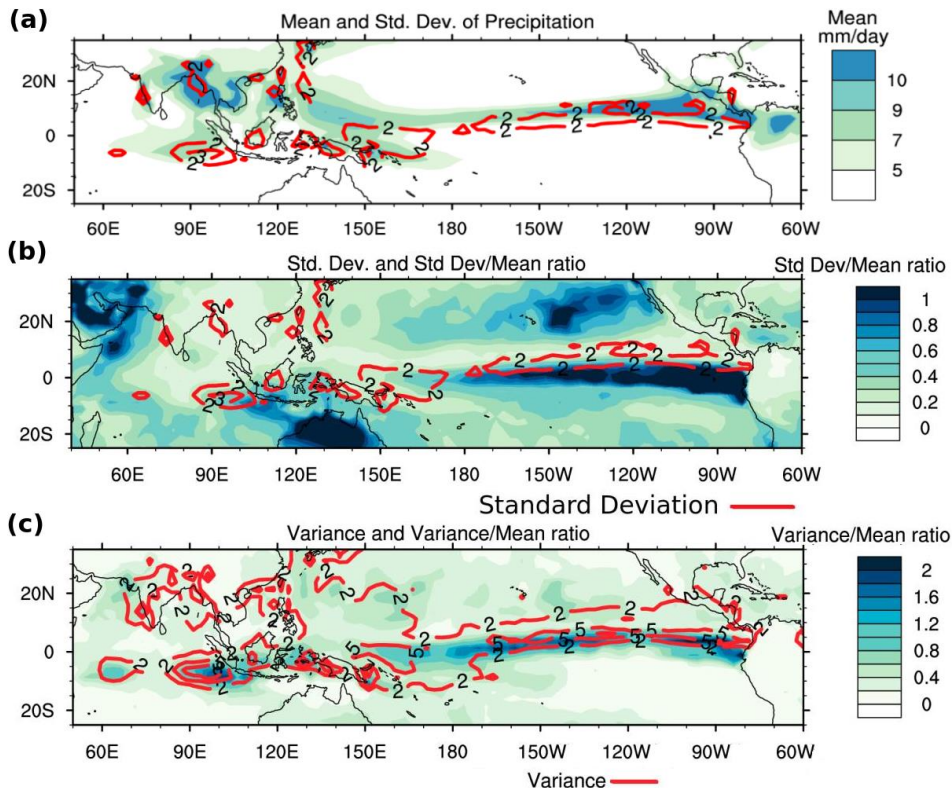
Figure 1: (a)JJAS climatological mean precipitation (shading) and standard deviation (contours) (b) Standard deviation (red contour) and standard deviation to mean ratio (shading) (c) Variance (red contour) and variance to mean ratio of precipitation (shading) from 41 years (1981-2021) of GPCP data.

The monsoon is an inherently coupled system (Webster et al., 2002; Ramu et al., 2016), and Indian Meteorological Department (IMD) has been using the Monsoon Mission Coupled Forecast System version 1 (MMCFSv1) model operationally to predict the ISM since 2011 (Benke et al., 2019). Indian Institute of Tropical Meteorology (IITM) has been using MMCFSv1 as a research testbed to study the various facets of ISM rainfall (ISMR) (Ramu et al., 2016; Krishna et al., 2019; Srivastava et al., 2021; Pillai et al., 2021; Pradhan et al., 2022; Rao et al., 2019). MMCFSv1 is based on a high-resolution Climate Forecast System model from National Centre for Environmental Prediction (NCEP) (Saha et al., 2014).

While the NCEP runs the model at a resolution of T126, IITM runs it at T382. Ramu et al., (2016) analyzed both the model resolutions (T126 and T382) based on 28 years hindcast to show that the skill of lower resolution model is 0.49 compared to the skill of 0.55 of the high-resolution model with the February initial conditions. Pillai et al., (2017) have shown that the potential predictability of ISMR is 0.7 in MMCFSv1, and the maximum actual skill (with different initial conditions) of the operational model at IMD (MMCFSv1) is 0.55. Hence, the gap between the potential predictability and actual skill is large. Many factors, such as resolution, initial conditions, physics, and dynamics, limit the models' skill. Coupled climate models' skill improvement involves efforts from many research groups specializing in a particular sub-domain (component) of the coupled model. As its components, the MMCFSv1 has a Global Forecast System atmospheric model with Eulerian dynamical core (GFS-EL, Moorthi et al., 2001), Modular Ocean model version 4 (MOM4, Griffies et al., 2004), and sea-ice model (SIS, Semtner, 1976; Winton, 2000), coupled together using a hard-coded coupler. This hard-

coded coupler runs on a single core. This presents a computational problem as the models grow in complexity and become highly parallelizable.

With an ever-increasing understanding of our climate system, the above-mentioned individual components of MMCFSv1 have seen a lot of improvements independently of each other. MOM6 (Adcroft, 2016) is a significant upgrade (algorithmically) over the MOM4 (discussed in detail in the next section). The predictability of the medium-range atmospheric models has improved with increasing model resolutions. The need for higher atmospheric model resolution emphasizes using a Semi-Lagrangian dynamical core in place of the Eulerian one (Staniforth et al., 1991). CICE5 (Bailey et al., 2018) is a separate code base designed to be used in coupled models and is highly parallelizable and brings in many improvements (see next section) over SIS (Semtner, 1976; Winton, 2000) sea ice model, which is a part of the MOM4 code base.

As mentioned above, the components in MMCFSv1 are hard coded to transfer and transform the data from one process (model component) to another through a coupler. To make any changes to the individual model component, one must understand how these model components are implemented and how the coupler accumulates, transfers, and regrids the boundary condition data from one component to another. However, since the coupler is hard coded to interface the individual model components, there is a lack of modularity in how MMCFSv1 is implemented.

Realizing this hinders seamless model development in coupled models, many groups across the climate community (Black et al., 2009; Craig et al., 2017; Balaji et al., 2004) have been developing the software infrastructure trying to bring modularity to the complicated climate model codes. The National Oceanic and Atmospheric Administration (NOAA) Environmental Modeling System (NEMS) is one such modelling framework (Black et al., 2009) which is used to streamline components of the models. NEMS architecture is based on the Earth Modeling System Framework (ESMF, Hill et al., 2004). ESMF standardizes how the model components interact with each other, thus bringing in modularity. NEMS refines the definition of what it means to be a model component and standardizes the initiation, running, and finalizing steps of each model component. MMCFSv2 uses the NEMS coupling framework and upgrades all the major individual model components of MMCFSv1 (Table 1). Using a NEMS coupler will facilitate easier future upgradation of MMCFSv2 components.

Systematic biases in MMCFSv1 were well documented (Ramu et al., 2016; Pillai et al., 2017), and the significant biases are the cooler SST (especially over the Indian and southern Pacific Ocean), dry bias over land, wet bias over the ocean, and weaker monsoon circulations. Hence, in this study, we have investigated the model's ability to simulate the mean state and assess the model's skill in predicting the phase and amplitude of ISMR. We have limited our simulations to the last 25 years (1998-2022) of retrospective hindcasts due to limitations in computational resources. The present paper gives details of MMCFSv2 individual component upgrades. We also analyze the simulated mean tropical SST, circulation, mean and interannual variability of ISMR and its teleconnection with different oceanic modes. Section 2 discusses model upgrades over MMCFSv1. Section 3 describes the experimental design for this study. We then show the simulated results and compare them with MMCFSv1 in section 4 before summarizing them in the last section.

Table 1 Major Changes to model components between MMCFSv1 to MMCFSv2

Model/Component	Atmosphere (resolution)	Ocean (resolution)	Ice model	Land Model	References
MMCFSv1	GFS-EL(T382, ~38km)	MOM4p0d (0.25 at 10S-10N)	SIS sea ice	NOAH-LSM	Moorthi et, al, 2001 *Griffies et al.,*

					2004
					Winton, 2000
					Ek et. Al 2003
MMCFSv2	GFS-SL (T574, ~38km)	MOM6 (0.125 at 10S-10N)	CICE5	NOAH-LSM	Sela, 2016 Adcroft 2016 Hunke et al., 2015 Ek et. Al 2003
Parameterizations	Cumulus	Ocean vertical grids	Ocean physical closures		
V1	SAS	Fixed (B-stensil)	Non-scale aware		
V2	New-SAS	Arbitrary Lagrangian Eulerian (C-stensil)	scale-aware parameterizations		
Horizontal Grid Size					
V1	1152x576	720x410	720x410	1152x576	
V2	1 152x576	1440x1080	1440x1080	1152x576	

90

4

2. MMCFSv2 model Details

We use the NCEP MMCFSv1 (Saha et al., 2014) as the base model to discuss the upgrades MMCFSv2 brings. The primary individual model components of MMCFSv1, upgraded in MMCFSv2, are tabulated in Table 1 and discussed briefly below. The MMCFSv1 uses the spectral model Global Forecast System (GFS) as the atmospheric model (Moorthi et al., 2001) with the Eulerian dynamical core. MMCFSv2 instead uses a Semi-Lagrangian dynamical core for the GFS (GFS-SL, Sela, 2010; Mukhopadhyay et al., 2019). Using a Semi-Lagrangian dynamical core allows us to have higher atmospheric model resolutions while keeping the time stepping the same.

2.1 MOM6 Ocean Model

MMCFSv1 uses the Geophysical Fluid Dynamics Laboratory Modular Ocean Model version 4p0d (MOM4) as the ocean model (Griffies et al., 2004). It has been upgraded to MOM6 (Adcroft, 2016) in MMCFSv2. MOM6 is based on generalized ocean dynamics which enables variable vertical and hybrid coordinates. Since MOM6 uses vertical Lagrangian remapping (Griffies et al., 2020), it can be configured with any vertical co-ordinates among geopotential, isopycnal, terrain-following, or hybrid (user-defined). Significant improvements brought by MOM6 over MOM4 include using C-grid stencil over B-grid stencil. C-grid stencil is preferred for simulations involving an active mesoscale eddy field. MOM6 uses scale-aware parameterizations for mesoscale eddy-permitting regimes is based on Jansen et al., (2019) and eddy fluxes are parameterized based on Jansen et al. (2015). Boundary layer scheme in MOM6 is based on Reichi et al., (2018) and incorporates Langmuir mixing. It also introduces a suite of parameterized mixing from breaking gravity waves. A new method for performing neutral diffusion is also introduced in MOM6 that prevents the spurious formation of extrema. Complete details of MOM6 can be found at https://www.gfdl.noaa.gov/mom-ocean-model/.

The present configuration of MOM6 used in MMCFSv2 consists of 40 vertical levels with HyCOM-like hybrid coordinates. The horizontal grid follows tripolar grid with poles over land and 1440 and 1080 points in x and y directions respectively. The resolution of the ocean component in MOM4 is 0.25 degrees between 10° S to 10° N latitude band and 0.5 degrees elsewhere. This has been increased to 0.125^o near the equator in MOM6. MOM6 is compiled with external coupler and a cap code (mom_cap.F90) interfaces the model to NEMS framework. The coupling happens every 30 minutes.

2.2 CICE5.0 Model

MMCFSv1 uses a three-layer (one layer of snow and two layers of sea ice) interactive sea ice model (Winton, 2000), which is an improvement over the Semtner three-layer model (Semtner, 1976). This component model has been upgraded to the Los Alamos CICE5 (Hunke et al., 2015) in MMCFSv2. CICE5 is designed to be used in coupled models and is highly parallelizable. The major improvements of CICE5 over the Sea-ice model of MMCFSv1 include ice velocity in atm-ice coupling updates and allowing a variable coefficient for the ice-ocean heat flux.

CICE5 is developed by LANL to be used in a fully coupled climate models. CICE5.0 has (improved/new) parameterizations for form drag, sea-ice biogeochemistry, explicit melt pond, among others. CICE5 has been extensively used in climate simulations by Community Earth System Model (CESM). More details can be found at CICE documentation (link in data availability section). CICE5 runs at MOM6 resolution of 1440 by 1080 points in the horizontal. Similar to MOM6, CICE5 code is coupled to NEMS framework using a cap code (cice_cap.F90) and the coupling happens every 30 minutes.

2.3 Coupler

The hard coded coupler in MMCFSv1 runs on a single processor and transfers surface fluxes (wind stress, and radiative) to the ocean model and provides SST to the atmospheric model after every coupling time step of 1800 seconds. This coupler has been replaced by NEMS coupler. This coupler is a parallel coupler and is currently running on 144 cores in MMCFSv2. More details on the NEMS coupler can be found in Black et al., (2009).

2.4 Other Model Components

As mentioned earlier, atmospheric component is based on GFS with semi-lagrangian dynamical core, Although the four-layer NOAH land surface model (Ek et al., 2003) remains the same between MMCFSv1 and MMCFSv2, the NEMS framework allows us to include newer versions of land models such as NOAH-MP. This will be done in future work.

3. Experimental Details and Observational/Reanalysis Data

The retrospective ensemble prediction (hindcast) runs of the MMCFSv1 have atmospheric horizontal resolutions corresponding to triangular truncation of T382L64, while that of MMCFSv2 is T574L64 (horizontal resolution of both versions is ~38km). The atmosphere, land, and ocean initial conditions for these runs are obtained from the NCEP Climate Forecast System Reanalysis (CFSR) (Saha et al. 2010). The atmospheric component of MMCFSv1 and MMCFSv2 has 64 sigma-pressure hybrid vertical levels, and the ocean component has 40 vertical layers. The convective parameterization scheme used in the atmospheric part of MMCFSv1 and MMCFSv2 is based on the Arakawa-Schubert scheme, with orographic gravity wave, drag, and momentum mixing.

Pillai et al. (2022) showed that the prediction skill for El Niño–Southern Oscillation (ENSO) was lower for MMCFSv1 initialized with February (3 months lead time) initial conditions compared to when it was initialized with April (1 month lead time) initial conditions. They showed that models which depend on ENSO teleconnection for ISMR interannual variability (MMCFSv1 in their case) have better ISMR prediction skills with April initial conditions. Hence, the MMCFSv2 experimental setup is based on a 10-member lagged ensemble with April initial conditions (00z01Apr, 12z01Apr, 00z06Apr, 12z06Apr, 00z11Apr, 12z11Apr, 00z16Apr, 12z16Apr, 00z21Apr, and 12z21Apr) while that of MMCFSv1 is like the one in Ramu et al. (2016), albeit, for April initial conditions and a total of 12 ensembles (2 additional ensembles corresponding to 00 and 12Z of 26th April). Each hindcast run is integrated for six months, from April to September. A total of 25 years of hindcasts have been performed from 1998 to 2022.

For the verification of the model-simulated rainfall, we use the Global Precipitation Climatology Project (GPCP, Adler et al. 2003) and 1-degree gridded daily rainfall from IMD (Rajeevan et al. 2006) for the same hindcast period (1998–2022). It may be noted that IMD uses data from variable rain gauge networks from day to day based on the availability of data from gauges. However, GPCP uses data from fixed rain gauge network. Since IMD keeps updating the rain gauge network continuously, the seasonal mean values also vary for each update (Pai et al. 2014). Hence, in this study, we use GPCP data as a standard product for assessing the skills of the ISMR. For sea surface temperature (SST) validation, we use the Extended Reconstructed Sea Surface Temperature (ERSST) version 5 (Huang et al. 2017, 2018, 2019, 2020). In addition, we also use ERA5 reanalysis products for winds (Hersbach et al. 2020). Model simulated mixed layer depth (MLD) was compared to CMCC Global Ocean Physical Reanalysis System (C-GLORS) MLD. We have used Pearson's test to compute the statistical significance of correlation coefficients and Student's t-test to compute the statistical significance of difference. Anomaly correlation coefficients (Phase skill) and Normalized Root Mean Square Error (normalized with standard deviation; amplitude skill) are used as a metric to assess the skill of the models in capturing ISMR and other tropical interannual modes.

4. Results

We first look at the ability of MMCFSv2 to simulate the mean tropical climatology of rainfall and surface temperature. We then look at the simulated large-scale circulation and interannual variability of ISMR before examining its teleconnections with different interannual modes in the tropics.

4.1 Climatology

4.1.1 Mean Rainfall

Most climate models (Pillai et al., 2018; Sabeerali et al., 2013) have shown that land rainfall is underestimated while rainfall over oceans is overestimated. Figure 2 shows JJAS mean precipitation from GPCP (observed) and the models. GPCP (Fig. 2 (a)) shows maximum rainfall over a band along the tropical Pacific Ocean. Both models simulate this tropical rain belt (Fig. 2 (b), (c)) reasonably well. Surprisingly, the dry bias over land, which is normally present in many of the climate models, is absent in MMCFSv2, except over the Indian land region. While the rainfall dry bias over west central India is increased the bias over northeast and east central India is reduced. MMCFSv1 has significant wet bias over the North Pacific, Atlantic and EIO regions (Fig. 2 (d)) which is significantly reduced in MMCFSv2 (Fig. 2 (e), (f)). MMCFSv2 is also closer to GPCP in Africa and south American regions.
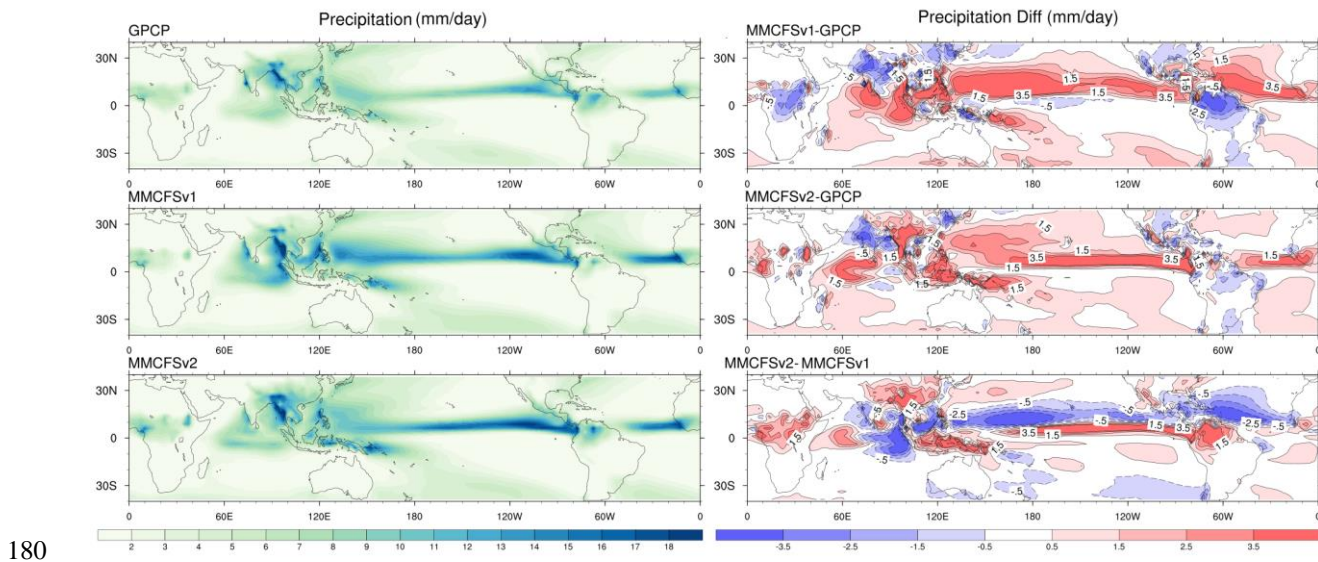
Figure 2: JJAS mean Rainfall (a) GPCP(b) MMCFSv1 (c) MMCFSv2, and bias (d) MMCFSv1-GPCP (e) MMCFSv2-GPCP, and (f) Difference between MMCFSv1 and MMCFSv2. Dashed contours are used for negative difference, while positive contours are solid.

Over the ISM region, there are three locations of precipitation maximum, viz, the head Bay of Bengal, the Western Ghats, and the southeastern equatorial Indian Ocean (Fig. 2 (a)). Both the models get these precipitation maxima (Fig. 2 (b), (c)). There is a strong wet bias over the Indian ocean basins and a dry bias over the northwest Indian landmass in MMCFSv1 (Fig. 2 (d)). This is significantly reduced in MMCFSv2. The dry bias over Indian landmass seen in both models is consistent with previous studies (Goswami et al., 2014; Saha et al., 2014; George et al., 2016; Ramu et al., 2016; Pillai et al., 2018). A study by Sabeerali et al., (2013) has reported similar precipitation bias in many CMIP5 models. Nevertheless, MMCFSv2 improves the dry bias over the Indian landmass over MMCFSv1 (Table 2). From recent CMIP6 models, the majority of the models also suffer from similar rainfall biases as MMCFSv1.
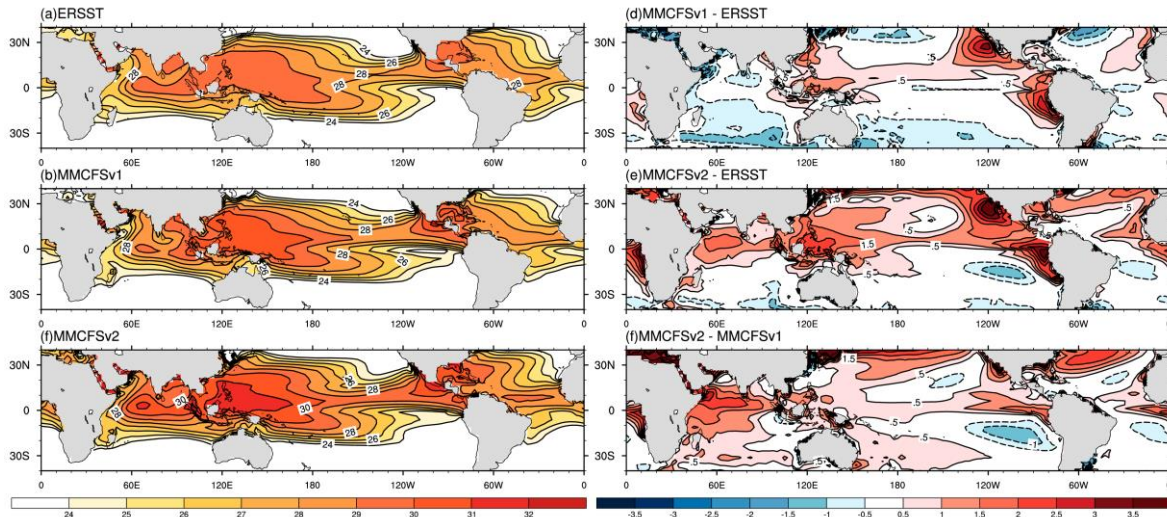
4.1.2 Temperature bias

Figure 3: JJAS mean Sea surface temperature (^{0}C) (a) ERSST (observed), (b) MMCFSv1 (c) MMCFSv2, and bias (d) MMCFSv1-ERSST (e) MMCFSv2-ERSST, and model difference (f) MMCFSv2 - MMCFSv1 over the tropics. Dashed contours are used for negative difference, while positive contours are solid.

The spatial distribution of observed (ERSST) and simulated (MMCFS) climatological JJAS mean SST is shown in Fig. 3. The presence of equatorial maxima characterizes the observed SST. The SST over the Indo-Pacific region is greater than 28° C and is known as the Indo-Pacific warm pool region (Fig. 3 (a), ERSST). Both models can simulate the large-scale distribution of tropical SST (Fig. 3 (b), (c)). MMCFSv1 shows a cold bias (greater than 0.5° C) over the tropical Indian Ocean (IO) and southern Pacific (Fig. 3 (d)). This cold bias has been reported previously by many studies (George et al., 2016; Pokhrel et al., 2012; Saha et al., 2014). It is shown to be due to the dry surface atmosphere and an associated increase in latent heat flux in MMCFSv1 by Pokhrel et al., (2012). MMCFSv1 also has a strong warm bias (of greater than 0.5-1.5° C) over the northwestern, southwestern, northeast, and southeast Pacific (Fig. 3 (d)). Zheng et al., (2011) reported that this strong warm bias over the northeast and southeast Pacific is due to the misrepresentation of stratus cloud decks and an associated increase in incoming short-wave radiation flux.

The cold SST bias of MMCFSv1 over the Indian Ocean is significantly reduced in MMCFSv2 (Fig. 3 (e)). MMCFSv2 has a warm bias (greater than 0.5° C) over the entire IO except for extreme southeast IO and Northern Arabian Sea (Fig. 3 (e)). The warm biases are intensified over Pacific region except southeastern Pacific in MMCFSv2 compared with MMCFSv1 (Fig.3 (f)). Overall, there is a warming of SSTs over tropics in MMCFSv2 compared to MMCFSv1. In fact, the latest CMIP6 models also have similar warm biases in SST (Farnetti et al., 2022)
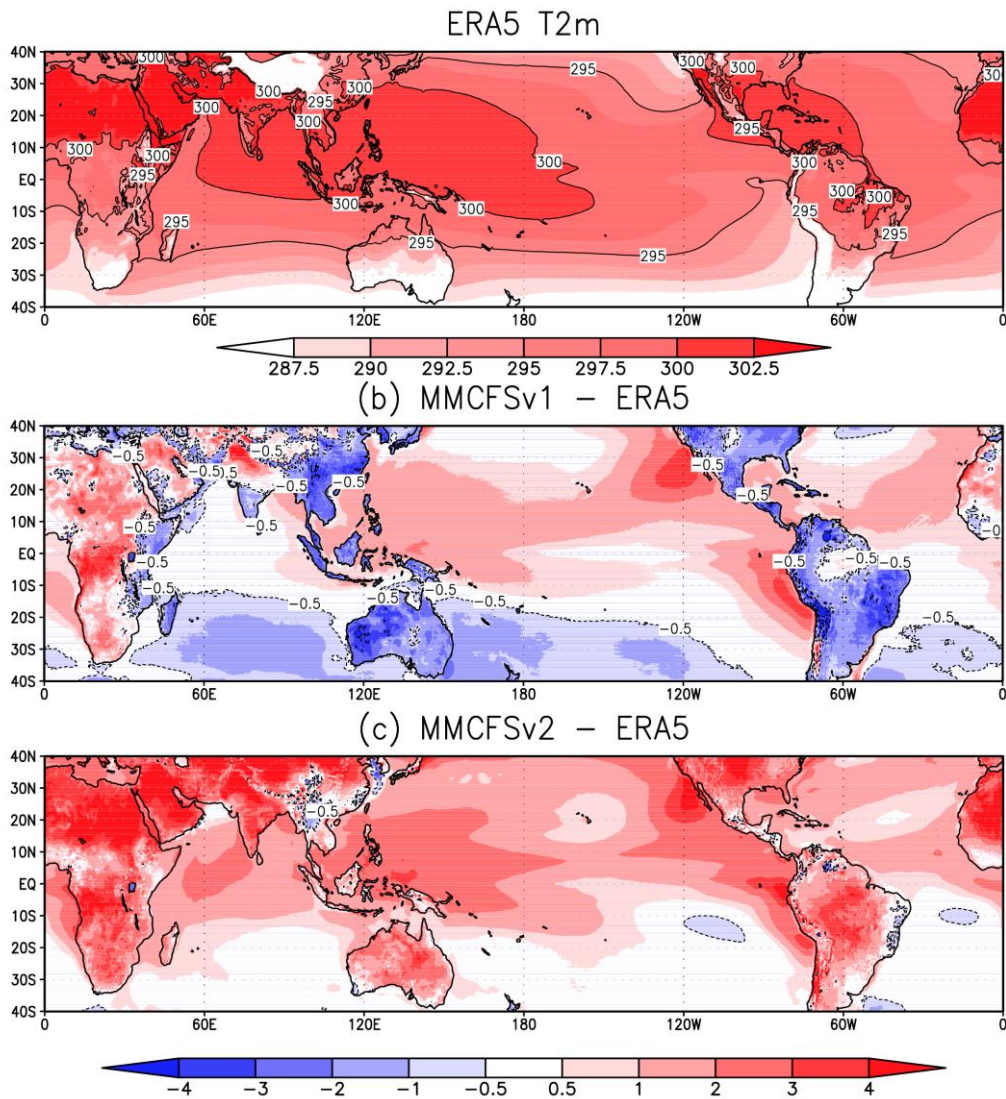
Figure 4: JJAS mean surface air temperature (K) at 2m (a) ERA5, bias (b) MMCFSv1-ERA5 (c) MMCFSv2-ERA5. Dashed contours are used for negative difference.

MMCFSv1 underestimates surface air (2 m) temperature (Fig. 7) over most of the land, including Tibetan Plateau, except the African region (overestimation by 2-4°C). MMCFSv2 overestimates surface air temperature over most of the tropics by more than 3° C. The warm SST bias in the tropics (Fig. 3) affects the surface air temperatures over oceans, and Fig. 4 shows the warmer 2m surface air temperature in MMCFSv2 compared to ERA5 and MMCFSv1. The cold bias of MMCFSv1 surface temperatures over the winter hemisphere (south of 15º S) has disappeared in MMCFSv2. The surface air warming is much more pronounced over the landmass.
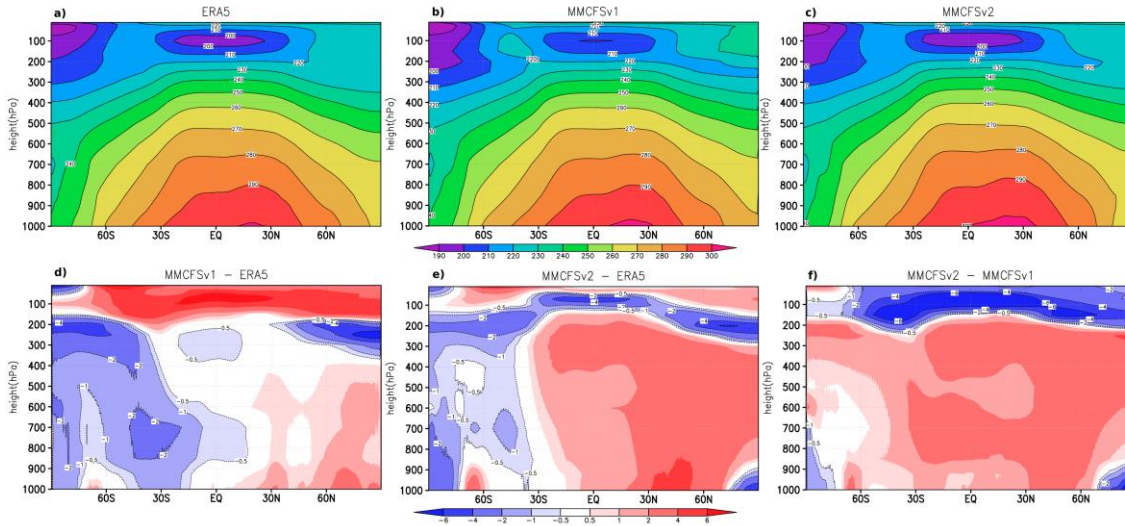
Figure 5: JJAS zonal mean temperature (K) (a) ERA5 (b) MMCFSv1 (c) MMCFSv2, bias (d) MMCFSv1-ERA5 (e)
MMCFSv2-ERA5, and (f) Difference between MMCFSv1 and MMCFSv2. Dashed contours (highlighted) are used for
negative difference.

The zonally averaged tropospheric air temperatures in Fig. 5 show both models simulating the mean observed structure
consistent with observations (Fig. 5 (a)-(c)). However, we can see that the surface warming seen in Fig. 4 produces warmer
columns in the MMCFSv2 compared to both observations and MMCFSv1 (Fig. 5 (d)-(f)). The warming, however, is confined
to the summer hemisphere and MMCFSv2 is closer to observations in the southern hemisphere than MMCFSv1. The most
significant upgrade from MMCFSv1 to MMCFSv2 is the ocean model. MOM6 has allowed us to use much higher ocean model
resolutions than MOM4. It has also allowed the use of scale-aware parameterizations for mesoscale eddy-permitting regimes.

Figure 6 shows the difference between simulated mixed layer depth by MMCFS (v1 and v2) and the Qnet into this
mixed layer. Except over equatorial Pacific Ocean (EPO), MMCFSv1 simulates deeper mixed layer depths compared to
observations (C-GLORS). MMCFSv2 improves on this bias of MMCFSv1 with significant reduction in MLD bias (< 10 m),
except over EPO, where the bias remains similar. Preliminary SST budget analysis showed that the shallower MLDs (Figure
6) compared to MMCFS1 and similar Qnet results in warmer SSTs in MMCFSv2. Considering the fact that satellite derived
SST accuracy is around 0.5 degrees (especially AVHRR, Ahmedabadi et al., 2009), a bias of 0.5 to 1 degree can not be
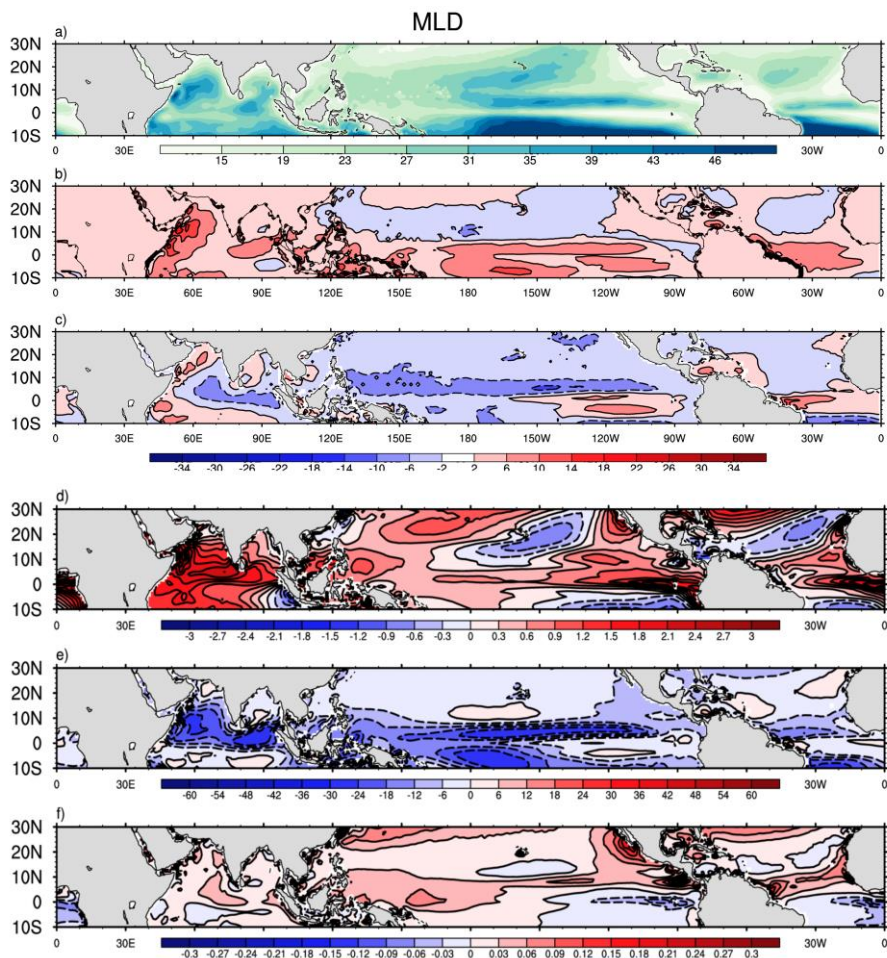considered as significant warm bias.

10

Figure 6. a) Mixed Layer Depth from C-GLORS, b) and c) Model bias of MLD from C_GLORS, d) SST difference between v2 and v1 (v2-v1) e) MLD difference (v2-v1) f) Qnet contribution to MLD. Dashed contours are used to highlight negative values.
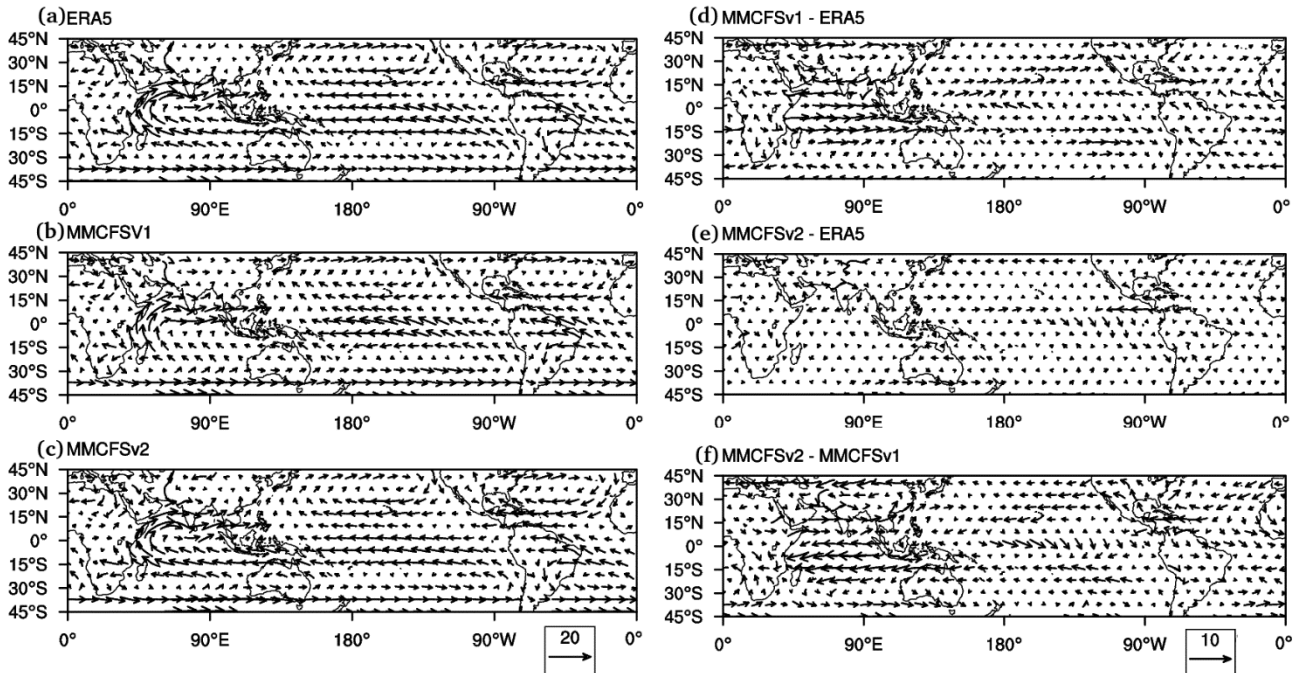
245

4.1.1 Winds

850hPa Winds

Figure 7: JJAS climatological mean winds (m/s) at 850 hPa (a) ERA5 (b) MMCFSv1 (c) MMCFSv2, bias (d) MMCFSv1-ERA5 (e) MMCFSv2-ERA5, and (f) Difference between MMCFSv2 and MMCFSv1.

JJAS mean lower tropospheric (850 hPa) observed (ERA5) and simulated (MMCFSv1 and MMCFSv2) winds in Fig. 7(a)-(c) show that both the models can capture the tropical convergence zone over the Pacific and Atlantic oceans well. Models can also simulate the observed monsoonal circulation (Fig. 7(a)) over the Indian region (60-90°E) reasonably well. The difference in 850 hPa winds (Fig. 7 (d), (e)) from ERA5 shows MMCFSv2 closer to it than MMCFSv1 over most of the tropics. MMCFSv2 winds are closer to ERA5, especially over the Indian Ocean region. A significant difference in winds can be seen between the two models over the Indian Ocean region (Fig. 7 (f)).

Focusing on the Indian region, a distinct feature of the ISM is the low-level jet (LLJ) over the Arabian Sea seen in 850 hPa winds (Fig. 7 (a)), also popularly known as the Findlater jet (Joseph 1966; Findlater 1969). Both models reproduce this low-level circulation (Fig. 7 (b, c)). The wind bias in Fig. 7 (d, e) shows that MMCFSv2 simulates the LLJ closer to observations than MMCFSv1. MMCFSv1 shows strong northeast/easterly wind bias over the southern Indian region, the Arabian Sea, and the Bay of Bengal. Significant westerly wind bias is seen in MMCFSv1 over the entire southern and equatorial Indian Ocean (Fig. 7). Figure 7 ((d), (e)) shows both models having a low-level anti-cyclonic circulation bias over the Indian subcontinent. Compared to MMCFSv1, the low-level anti-cyclonic circulation bias is significantly reduced in MMCFSv2 (Fig. 7 (e), (f)). MMCFSv1 simulates stronger northeasterly or easterly wind bias compared to MMCFSv2 (Fig.7 (f)) over the equatorial region. This may be due to the enhanced convection in the eastern equatorial Indian Ocean in MMCFSv2 (Fig. 2).
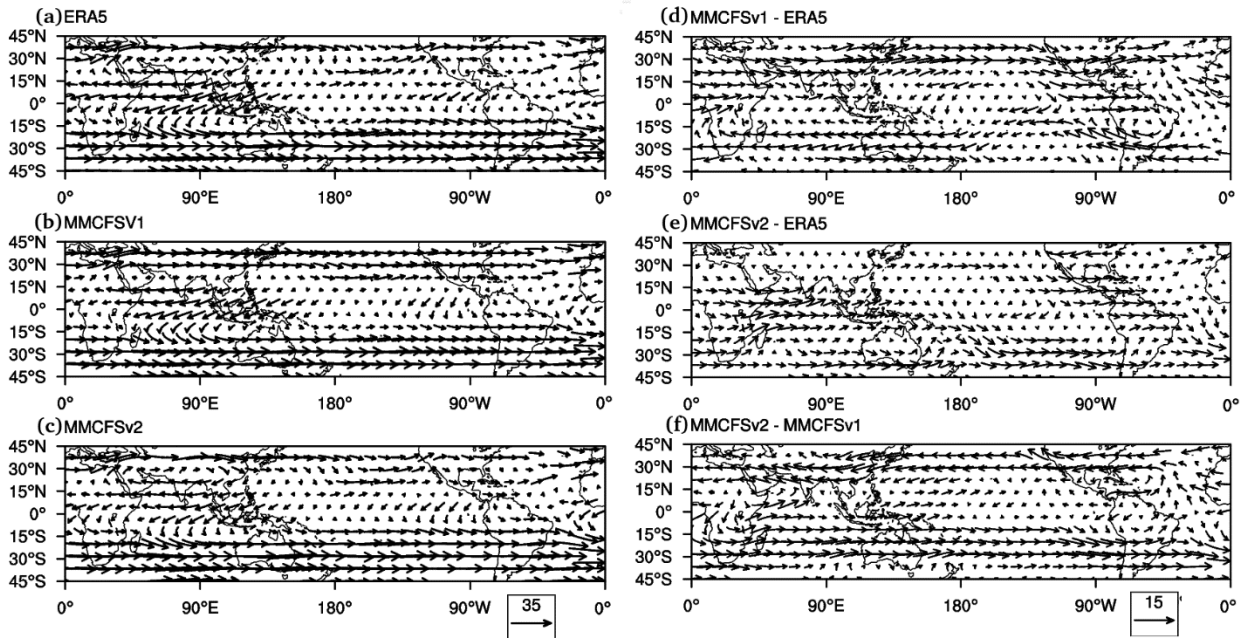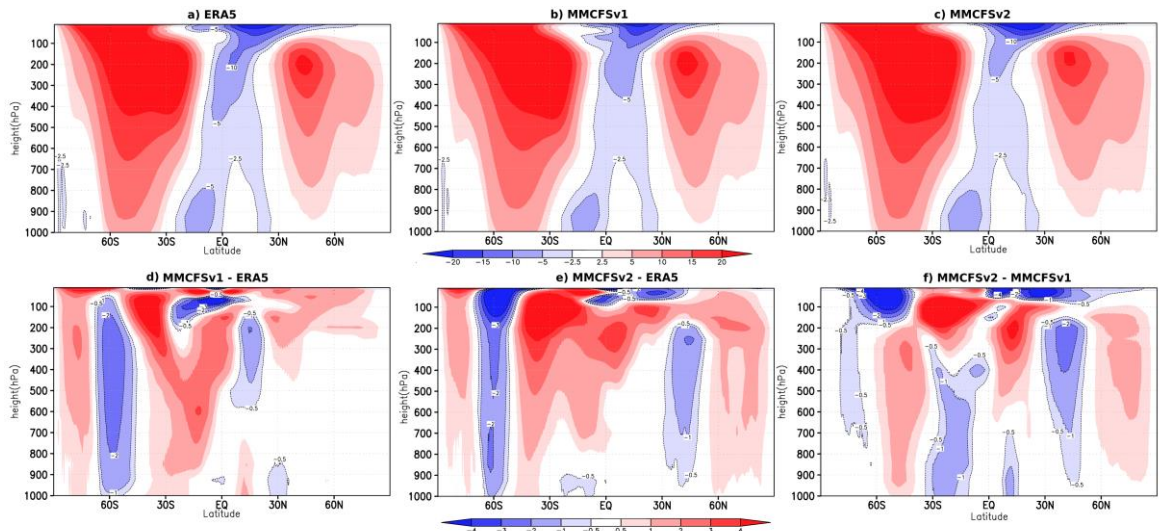
200hPa Winds

Figure 8: JJAS climatological mean winds (m/s) 200 hPa (a) ERA5 (b) MMCFSv1 (c) MMCFSv2, and bias (d) MMCFSv1-ERA5 (e) MMCFSv2-ERA5, and (f) Difference between MMCFSv2 and MMCFSv1.

270   Both models simulate the observed upper tropospheric tropical divergence and subtropical jets (in 200 hPa winds, Fig. 8 (a)-(c)). The monsoonal circulation over the Indian region is also evident in both models. The difference in 200 hPa winds (Fig. 8 (d), (e)) shows MMCFSv1 winds are closer to ERA5 over the Indian oceanic region (15° S-15° N), and MMCFSv2's winds are closer to ERA5 over Asian landmass (north of 15° N). MMCFSv2 simulates a weaker (stronger) subtropical jet over the northern (southern) hemisphere compared to MMCFSv1 and is closer to ERA5. Significant differences in 200 hPa
275   winds can be seen between the two models over the Indian landmass, Indian Ocean, Southern Pacific, and Atlantic oceanic region. The mean upper tropospheric (200 hPa) winds during ISM are characterized by the Tropical Easterly Jet (TEJ) and Tibetan anticyclone (Fig.8 (a)) (Krishnamurti et al. 1976). Both models can get these upper tropospheric circulation features (Fig. 8 (b), (c)). Compared to MMCFSv1, MMCFSv2 has a weaker westerly bias over India (Fig. 8 (d)-(f)).

13

Figure 9: JJAS climatological zonal mean wind (m/s) (a) ERA5 (b) MMCFSv1 (c) MMCFSv2, bias (d) MMCFSv1-ERA5 (e) MMCFSv2-ERA5, and (f) Difference between MMCFSv1 and MMCFSv2. Negative contours are highlighted with contour lines.

Fig. 9 (a) shows the longitudinally (global) averaged zonal (U) winds from ERA5. The models capture the easterly jet in the tropical convergence zone and the westerly jets in the mid-latitudes (Fig. 9 (b), (c)). MMCFSv1 simulated wind bias (Fig. 9 (d)) shows reduced strength of easterlies in the southern tropics and westerlies in the southern mid-latitudes. MMCFSv2 shows (Fig. 9 (e)) a weaker strength in the mid and upper tropospheric region of the tropical easterly jet. A weaker westerly jet in MMCFSv2 can be seen at both 50-60N and 60S. The winds in the northern hemisphere are close to ERA5 in MMCFSv1. The tropical surface zonal winds close to ERA5 in MMCFSv2.

Comparing the two simulated winds with each other (Fig. 9 (f)), we see a slightly reduced strength of the upper-level westerly jet in the summer hemisphere (45N, 200-500 hPa in Fig. 9 (f)) and increased strength in the winter hemisphere (45S, 200-900 hPa) in MMCFSv2 compared to MMCFSv1. Overall, both models reasonably simulate the zonal mean tropical winds, with slightly different strengths of tropical and sub-tropical jets. Since ISM is significantly affected by ENSO through Hadley cell, we expect significantly different teleconnection patterns between ISMR and ENSO in the two models (Fig. 14 discussed later). This also encourages us to look at the wind shear structure simulated by the two models.
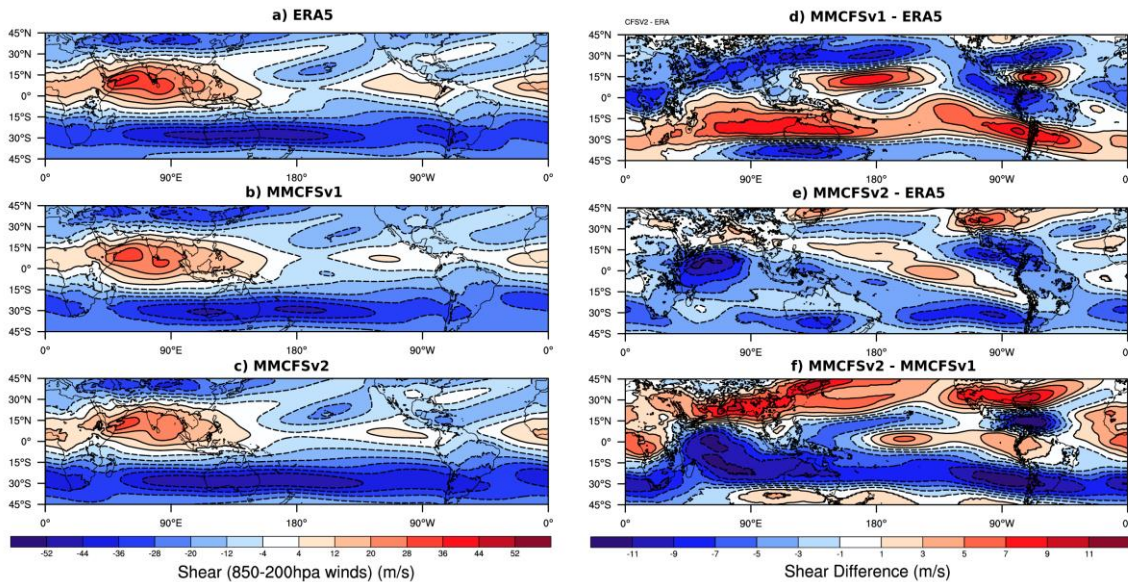
4.1.2 Wind Shear

Figure 10: JJAS seasonal mean easterly wind shear (U850–U200, m/s) in (a) observations (ERA5) (b) MMCFSv1, and (c) MMCFSv2. Seasonal mean easterly wind shear biases (model-observation) in (d) MMCFSv1 (e) MMCFSv2. (f) Difference in simulated seasonal mean easterly wind shear between MMCFSv2 and MMCFSv1 hindcast runs. Dashed contours are used for negative values while solid contours are positive values.

The vertical wind shear over the Asian Summer monsoon (ASM) region plays an important role in modulating the northward propagation of monsoon intraseasonal oscillations (MISO) (Jiang et al. 2004). Figure 10 shows the observed and the model-simulated JJAS seasonal mean of easterly wind shear. The wind shear is computed as the difference between 850 hPa and 200 hPa zonal (U) winds. Large positive wind shear is observed (Fig. 10 (a)) over the South Asian region (greater than 12 m/s) during the monsoon season. Positive wind shear is also seen over the Sub-Saharan region, the Indian Ocean, the West and East Pacific, and Equatorial Atlantic regions. Negative wind shear is observed in central North, South Pacific, and North Atlantic oceanic regions. Both models capture these features well (Fig. 10 (b), (c)). The wind shear bias (Fig. 10 (d), (e)) shows that MMCFSv2 shear is closer to ERA5 (difference less than 5 m/s) compared to MMCFSv1 (difference greater than 5 m/s) over most of the tropical regions. MMCFSv1 largely simulates a high negative bias over the Northern hemisphere and positive bias over the Southern hemisphere (Fig. 10 (d)), which has improved significantly in MMCFSv2 (Fig. 10 (e)). The bias in MMCFSv2 is significantly lower compared to MMCFSv1 over Asian and African landmass and most of the Pacific and Atlantic oceans.

ERA5 reanalysis shows a positive wind shear over the ASM domain (Fig. 10 (a)). The wind shear over the ASM region is underestimated in MMCFSv1 and MMCFSv2 (Figure 10 (b), (c)), consistent with the weak monsoon winds and TEJ, as seen in Fig. 7 and 8. However, there is a considerable difference between the two models. Whereas MMCFSv1 produces a large negative bias over Indian land and a positive bias over the southern Indian ocean compared to observations (Fig. 10 (d)), MMCFSv2 bias is positive over Indian land and predominantly negative over the Indian oceanic region. This difference between the simulations is much clearer in Fig. 10 (f). Therefore, there will be a considerable difference between the northward propagation speeds of the MISOs of MMCFSv1 and MMCFSv2. The difference in MISOs characteristics

15

will be explored in greater detail in a future study. MMCFSv2 underestimates shear in the western equatorial Indian Ocean/Arabian Sea, primarily due to a simulated weak easterly jet at 200 hPa (Fig. 8)

4.1.3 Interannual variability of ISMR and Potential Skill

The year-to-year variations of the area-averaged JJAS rainfall over the Indian land region are shown in Fig. 10. The observed all-India summer monsoon rainfall time series is prepared from the India Meteorological Department (IMD) gridded land rainfall and GPCP rainfall data. Figure 10 shows that both models can capture the recent rainfall deficit years of 2014 and 2015, as can be seen from GPCP. Out of 25 re-forecast years, MMCFSv2 could capture 20 years correctly, while MMCFSv1 could capture 15 years. Failure of the hindcasts in 2019 and 2000 is required to be analyzed in detail. A detailed analysis is required to understand the performance of the MMCFSv2.
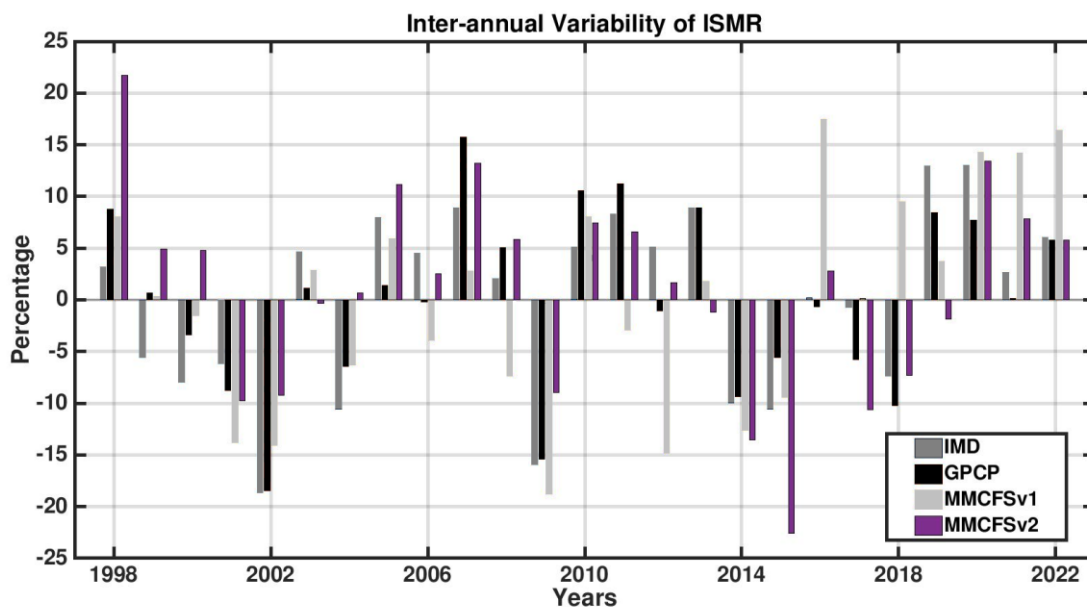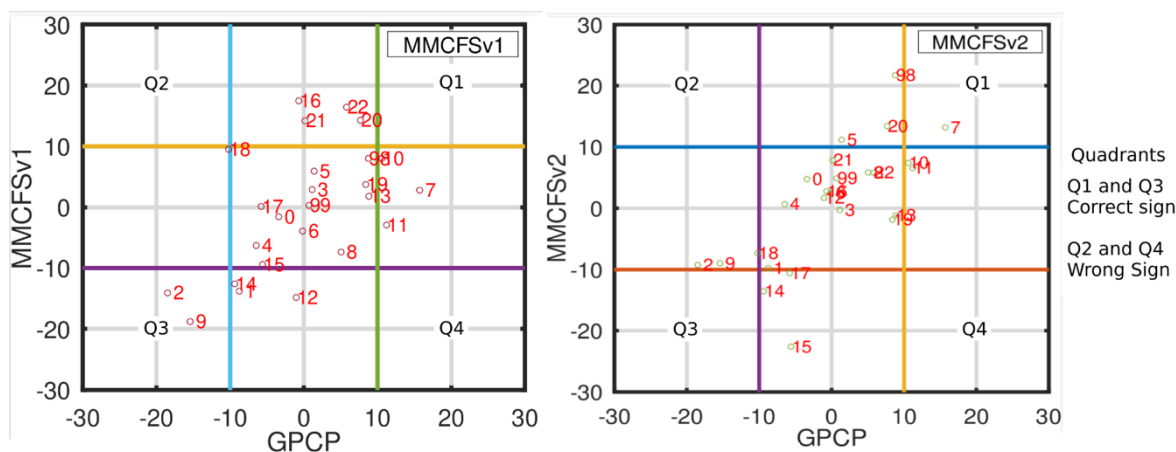

Figure 11: Interannual Variability of area averaged rainfall over Indian land mass from model hindcast (MMCFSv2, MMCFSv1) and different observational datasets (IMD and GPCP).

Table 2 summarizes the model skill in reproducing interannual variability of observed ISMR during 1998-2022. MMCFSv2 shows improvements in producing the mean of JJAS rainfall over MMCFSv1 by reducing the dry bias from 1.32 to 1.04 mm/day (~4 %) with respect to GPCP. MMCFSv2 captures the phase of interannual variability with a higher skill of 0.72 over 0.55 of MMCFSv1 when GPCP is considered as observation. Hence, MMCFSv2 improves the phase skill by 17 %.

16

Table 2. Mean ISMR, the standard deviation of ISMR, Bias from observations, Anomaly correlation coefficient (skill), Root mean square error of percentage departure, and Normalized (with std. Deviation) RMSE for 1998-2022. Correlation values above 99 % are shown in bold.

ISMR Characteristics						
Data from	Mean (mm/day)	STD (mm/day)	Bias (mm/day)	Skill	RMSE	NRMSE
Observations						
GPCP	6.99	0.61				
IMD	7.01	0.62				
Models						
MMCFSv2	5.95	0.58				
vs IMD			-1.06	**0.63**	**7.98%**	**0.92**
vs. GPCP			-1.04	**0.72**	**7.01%**	**0.82**
MMCFSv1	5.67	0.59				
vs. IMD			-1.34	**0.58**	**8.74%**	**1.0**
vs. GPCP			-1.32	**0.55**	**8.99%**	**1.06**

Figure 12. Scatter plot of ISMR anomaly (percentage) from GPCP (x-axis), and MMCFS (y-axis), left panel is MMCFSv1 and right panel is MMCFSv2.

From the scatter plot it is evident that many observed normal years were predicted as extremes in v1. Hence, we calculated the false alarm rates and the hit rates for both the models. We used two criteria for defining normal years, viz 10% and 5% departure from the climatological mean. Table 5 in the supplement summarizes the false alarms and hit rates. As seen from the table, MMCFSv1 has a higher false alarm rate and a lower hit rate than MMCFSv2.

GPCP	10% departure			GPCP	5% departure	
Normal Years	V1	False Alarm		Normal Years	V1	False Alarm
19		7		8		4
Excess		Hit Rate		Excess		Hit Rate
3		2		9		10
Drought	V2	False Alarm		Drought	V2	False Alarm
3		5		8		2
Total Extreme Years		Hit Rate		Total Extreme Years		Hit Rate
6		2		17		14

Table 3. Summarizing observed normal, excess, and drought years (first column uses 10% departure from mean, and third column uses 5% departure from the mean to define extreme years). The second (10%) and the fourth column (5%) summarizes hit rates and false alarms from v1 and v2 of MMCFS.

Pillai et al., (2018) compared the seasonal prediction skill of ISMR in MMCFSv1 (T382) with the US National Multi-Model Ensemble (NMME) project for the simulation years of 1981-2009. They found that MMCFSv1 has better skill in reproducing interannual variability of ISMR (ACC=0.55) compared to the other NMME models (ACC<0.4) and MMCFSv1 is better at simulating the observed standard deviation of ISMR. The Taylor diagram (Taylor, 2000) in Fig. 13 compares the skill of MMCFS (v1 and v2), and NMME models in reproducing observed Standard Deviation (SD, normalized), Root Mean Squared Error normalized with observed standard deviation (NRMSE). *Of these NMME models, GFDL_FLORA, GFDL_FLORB, and SPISV2 have data for the years of 1998-2021. We found that removal of year 2022 from other models does not change the scores significantly.* There are five models which simulate the observed SD reasonably well (normalized SD approximately 1.0), viz. *MMCFSv2, GFDL_Aero, SIPSv2, SPSIC3, GMAO*. All the other models have larger or smaller standard deviations with respect to observations. A 10 % deviation from the climatological mean is sufficient to have an excess or a drought monsoon over India (Singh et al., 2015). Hence, getting the NRMSE below 1.0 is crucial. Two models which stand out in terms of NRMSE are MMCFSv2 (0.82) and GFDL_Aero (0.85). All the other models simulate NRMSE larger than 0.85. MMCFSv2 reduces the NRMSE from 1.04 of MMCFSv1 to 0.82 with respect to GPCP, which is about 20 %. GFDL_Aero also has a lower ACC of 0.53 compared to 0.72 of MMCFSv2. MMCFSv2 has the highest skill in capturing the interannual variability of ISMR compared to all the other models. Hence, in terms of SD, NRMSE, and the ACC, MMCFSv2 stands out compared to all the other NMME models and the MMCFSv1.
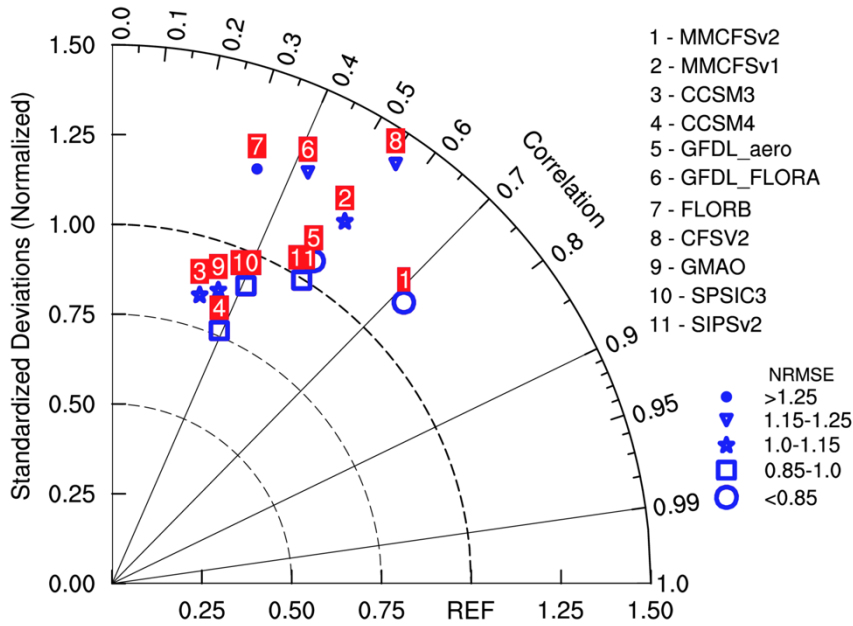
Figure 13: Taylor diagram showing the Normalized RMSE, pattern correlation coefficients and normalized standard deviation of the JJAS mean ISMR of MMCFS and NMME models with respect to GPCP observations. NMME Models simulation duration is 1998-2021. MMCFS is from 1998-2022.

380   The uncertainty in initial conditions is inevitable due to gaps in observational networks and the limitations of data assimilation systems. Therefore, it is not possible to know the "true" state of the earth system, which serves as a starting point for the seasonal simulations. Ensemble forecasting techniques (such as the one used in this study) are employed to account for the initial state's uncertainty. If we assume the model is perfect, the uncertainty in initial conditions puts an upper limit to predictability. This upper limit is termed as the potential predictability and estimates the maximum skill the "perfect" model

385   can achieve. Let us say that the forecast for the variable "x" using the initial condition "i" has a probability distribution P (x|i). This forecast reaches an equilibrium state asymptotically with the distribution q(x). The distance between these two distributions is a measure of predictability and is termed as the relative entropy (RE) or the *Kullback-Leibler* distance. If this forecast distribution is identical to the climatological distribution, there is no predictability. RE can be estimated using the following expression, following Kleeman (2002), under the assumption that both the distributions are gaussian:

390
$$RE = \frac{1}{2}\left[\ln\left(\frac{\sigma_x^2}{\sigma_{x|i}^2}\right) + \frac{\sigma_{x|i}^2}{\sigma_x^2} + \frac{\left(\mu_{x|i} - \mu_x\right)^2}{\sigma_x^2} - 1\right]$$

where $\sigma_{x|i}^2$ and σ_x^2 are the ensemble (forecast) and climatological variance, respectively. μ_x and $\mu_{x|i}$ are the climatological and ensemble mean, respectively. Climatological variance is estimated as the sum of signal and noise variance (Delsole and Tippett, 2007) as:

19

$$\sigma_x^2 \; = \; \frac{1}{N} \sum_{i=1}^{N} \sigma_{x|i}^2 + \frac{1}{N} \sum_{i=1}^{N} \left(\mu_{x|i} - \mu_x \right)^2$$

Average of RE across all ensembles is the Mutual Information (MI). Potential skill is defined as:

$$PS = \; \sqrt{1 - e^{(-2\,MI)}}$$

The actual skill achieved by the model in this paper is computed using the anomaly correlation coefficient. PS for MMCFSv2 is 0.79 using the above expression, while the actual skill obtained is 0.72 (Table 2). PS and actual skill for MMCFSv1 for
400   1981-2017 is 0.72 and 0.38, respectively (Pillai et al., 2018). This indicates that the actual model skill of MMCFSv2 is very close to the perfect model skill. Further improvements to the individual model components shall bring the actual skill closer to the potential skill.

Recent studies (Ramu et al., 2016; George et al., 2016; Pillai et al., 2016, 2022) have shown that the seasonal prediction skill of monsoon in MMCFSv1 is significantly impacted by the El Niño-Southern Oscillation (ENSO)-monsoon relationship.
405   MMCFSv1 also has some limitations in representing the relationship between Indian Ocean SST and monsoon. We, therefore, now analyze the simulated teleconnections of the observed and simulated ISMR with different oceanic regions over the world.

4.2 Teleconnections

Earlier studies have found that the year-to-year variability of ISMR is mainly linked to the Pacific ENSO and Indian
410   Ocean Dipole (IOD) (Webster et al., 1992; Kumar et al., 1999; Saji et al., 1999; Ashok et al., 2004; Rajeevan et al., 2007a, 2007b). Atlantic zonal and meridional modes (AZM and AMM) also play a role in modulating ISMR. AZM is the oscillatory normal mode (zonal) seen in the principal oscillation pattern analysis of SST (Ding et al., 2010; Zebiak, 1993), while AMM refers to the leading maximum covariance analysis mode in the tropical Atlantic. IOD is the difference in sea surface temperature between western and eastern equatorial Indian ocean.

415   Recently, Sabeerali et al., (2019) explored the impact of the Atlantic zonal mode on ISM at inter-annual time scales in recent years using CFSv2. Here, we compare the ability of the models to simulate the teleconnections between ISM and ENSO, IOD, and the Atlantic modes. Table 4 summarizes the skill of models in simulating the oceanic modes (ENSO, eastern Indian ocean dipole (EIOD), AMM, and AZM) and their teleconnections with ISMR. Here, only the eastern pole of the IOD is considered, as it is the stationary part of the IOD (Rao et al., 2009).

420   **Table 4:** Teleconnections of ISMR with different oceanic Indices and skill of the models in capturing these modes (95% statistically significant values in bold)

Teleconnection (with ISMR)	Nino 3.4	EIOD	AMM	AZM
Observations	**-0.64**	-0.04	0.18	0.19
MMCFSv2	**-0.75**	0.33	-0.07	**0.46**
MMCFSv1	**-0.83**	**0.68**	0.35	0.08
SKILL	Nino3.4	EIO	AMM	AZM
MMCFSv2	**0.83**	**0.42**	0.15	0.32
MMCFSv1	**0.82**	**0.58**	0.01	0.13

4.2.1 ENSO
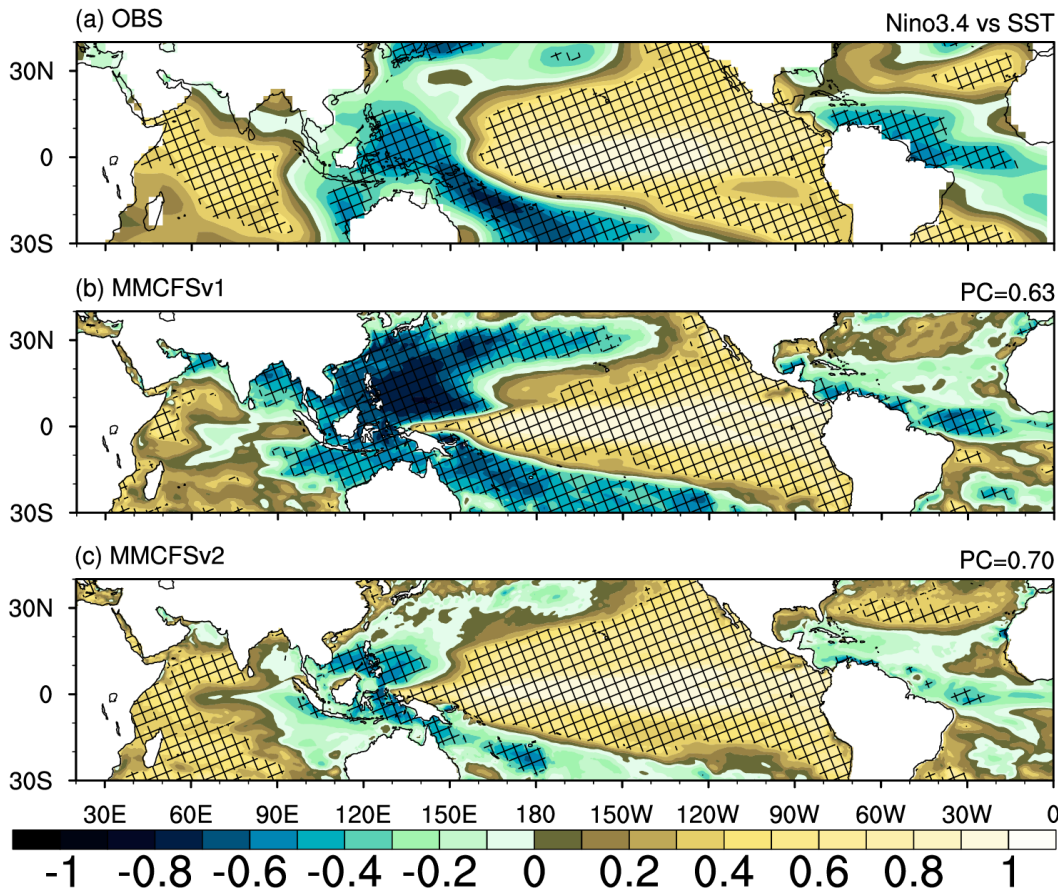
Figure 14: Correlation between JJAS Nino 3.4 (index) SST anomalies and Tropical SST anomalies in (a) Observations (ERSST), (b) MMCFSv1, and (c) MMCFSv2. The hatching shows statistical significance at 95 % confidence level.

Models can capture Nino 3.4 with high skill (Table 4). The spatial distribution of simultaneous correlations between Nino 3.4 SST anomalies (index) and tropical SST anomalies in JJAS are shown in Fig. 14. Positive correlations over the eastern/central tropical Pacific and western/central Indian Ocean are observed. Moreover, negative correlations are observed over the western tropical Pacific, eastern equatorial Indian Ocean, and tropical Atlantic Ocean (Fig. 14 (a)). MMCFSv2 simulates these large-scale teleconnection patterns associated with Nino 3.4 over the tropics with a higher pattern correlation of 0.70 than MMCFSv1 (PC=0.63) (Fig. 14 (b), (c)). In MMCFSv1, positive correlations over the Pacific and western Indian

21

oceans are weaker than observations. MMCFSv2, on the other hand, captures these teleconnection patterns in the tropical
440 Indian Ocean and over the Pacific regions reasonably well; hence pattern correlation is higher for MMCFv2.
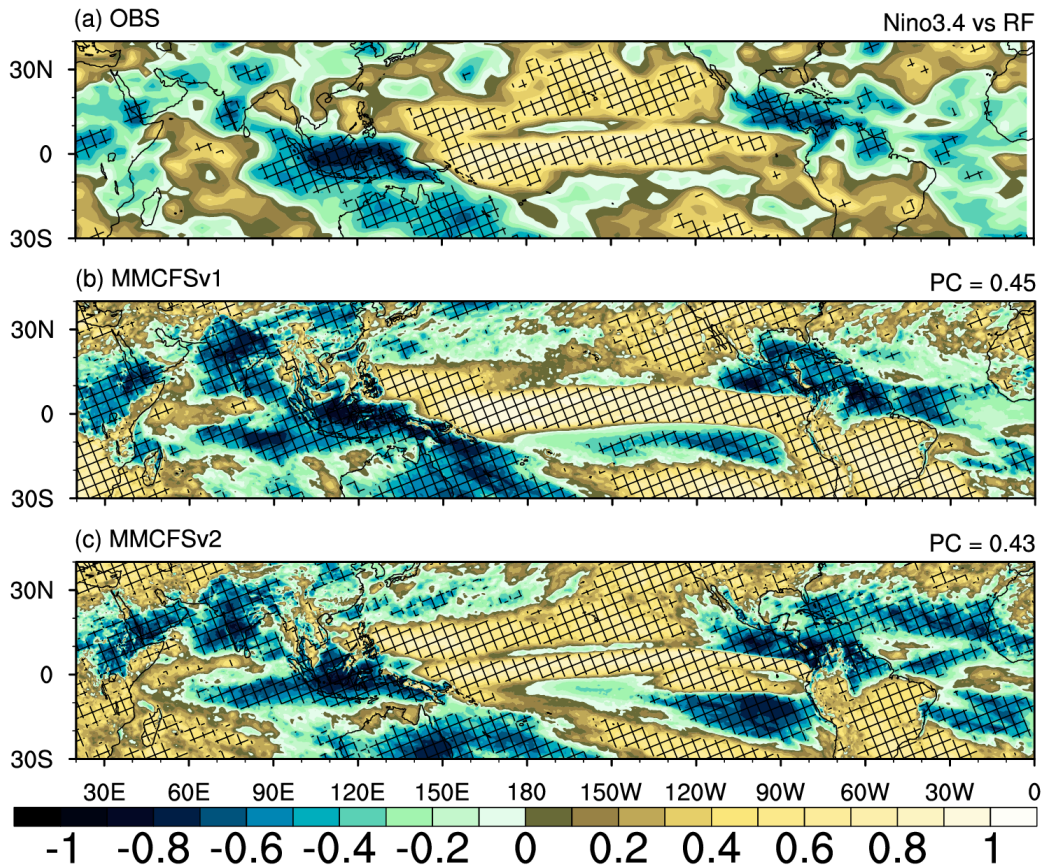

Figure 15: Correlation between JJAS Nino 3.4 (index) SST anomalies and Tropical rainfall anomalies in (a) observations
(GPCP), (b) MMCFSv1, and (c) MMCFSv2. The hatching shows statistically significant at 95% confidence level.

445   The spatial plot of the correlation between the boreal summer Nino 3.4 anomaly index and rainfall anomaly over the
tropical region is shown in Fig. 15. Observations show that the Nino 3.4 SST anomalies are negatively correlated (CC of -
0.64, Fig. 15 (a) and Table 4) with rainfall over the Indian land region (Fig. 15 (a)). Consistent with observations, both
MMCFSv1 and MMCFSv2 simulate this inverse relationship reasonably well, albeit with an overestimation. Nino 3.4 and
ISMR teleconnection in MMCFSv2 (-0.75) is closer to observations (-0.64) than in MMCFSv1 (-0.83). Additionally,
450 observations show a strong positive correlation between the Nino 3.4 SST anomalies and rainfall over the tropical Pacific.
MMCFSv2 can and MMCFSv1 cannot simulate this positive correlation over the north Pacific region (Fig. 15 (b), (c)). A
moderate negative correlation is seen over the Atlantic Ocean (Fig. 15 (a)), which is better captured by MMCFSv1. Except
over the southeast equatorial Pacific and Atlantic Oceans, MMCFSv2 can reproduce the Nino3.4 induced rainfall pattern

22

over the Bay of Bengal region and North and equatorial Pacific. Both models can capture the correlations over the Indian Ocean, with a slightly over-estimated Nino3.4 induced rainfall pattern (Fig. 15 (b), (c)).

4.2.2 EIOD and other Tropical modes

MMCFSv1 has a higher skill of 0.58 in capturing EIOD than MMCFSv2 (0.42, from Table 4). The spatial pattern of correlation between ERSST over the EIOD box (10° S to the Equator, 90-110° E) and tropical SSTs anomalies during JJAS season is shown in Fig. 16. Here, only the eastern pole of the IOD is considered as it is the stationary part of the IOD (Rao et al., 2009). Observations show a strong positive correlation between the Indo-Pacific warm pool region and the equatorial Atlantic Ocean. Negative correlations exist between the tropical Pacific Ocean and the western tropical Indian Ocean (Fig. 16 (a)). The pattern correlation of this teleconnection has improved from 0.31 in MMCFSv1 to 0.38 in MMCFSv2. Both models capture the positive correlations over the Indo-Pacific warm pool region (Fig.3 (b), (c)). MMCFSv1 simulates a basin-wide positive correlation over the eastern Indian Ocean (Fig.16 (c)) in contrast to the observed negative correlation pattern (Fig.16 (b)). It is also unable to capture the teleconnection pattern over the northern Pacific. MMCFSv2 captures these teleconnection patterns over the tropical Oceans and the eastern Indian Ocean (Fig. 16 (c)).
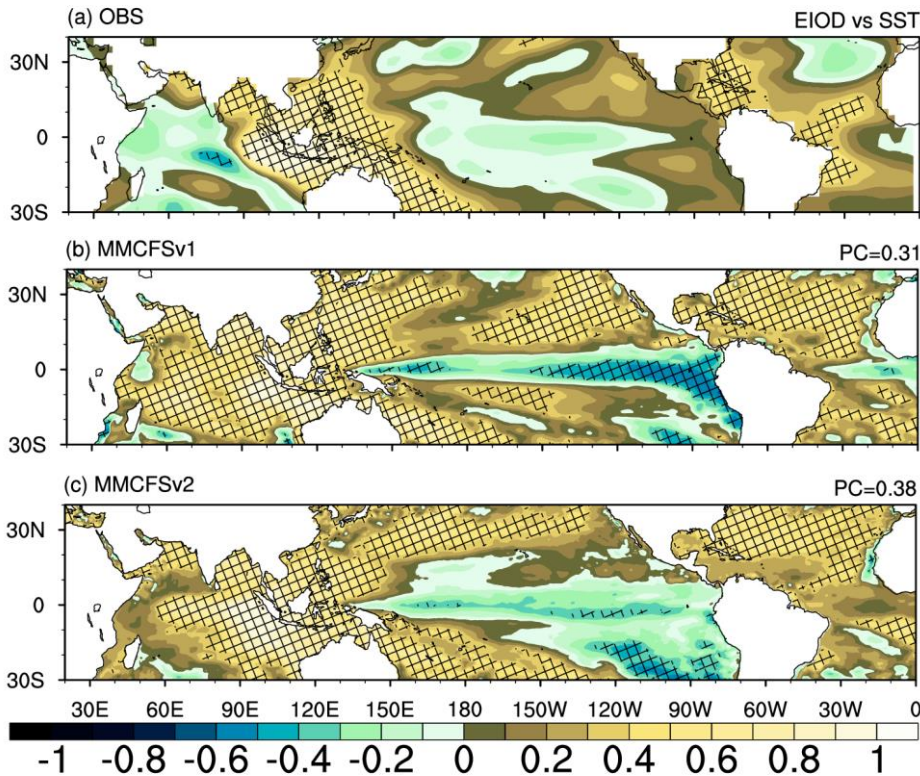

Figure 16: Correlation between SST over the eastern IOD box (10° S to equator, 90-110° E) and tropical SSTs anomalies during JJAS. (a) Observations (ERSST), (b) MMCFSv1, and (c) MMCFSv2. The hatching shows statistically significant at 95 % confidence level.

Figure 17 shows the spatial map of the correlation between the SST anomalies over the eastern equatorial Indian Ocean and rainfall anomalies over the tropical region. A positive correlation (not significant) in most parts of south/central India is observed. An expected strong positive correlation exists over the eastern Indian Ocean and north of Australia. Pacific and Atlantic Oceanic rainfall has a weak correlation with eastern equatorial Indian Ocean SST anomalies (Fig. 17). MMCFSv2 simulates this EIOD-induced rainfall pattern over the central and southern Indian regions. It is, however, the opposite of the observed relation over the northern Indian Ocean region (Fig. 17 (b)). MMCFSv1 overestimates this positive correlation over the Indian region compared to MMCFSv2. The pattern correlation between these teleconnections (EIOD SST-rainfall, Fig. 17) has improved from 0.13 in MMCFSv1 to 0.24 in MMCFSv2. The observed teleconnection between ISMR and EIOD is -0.04 (Table 4). On the contrary, MMCFSv2 and MMCFSv1 show a strong positive teleconnection relationship between ISMR and IOD of 0.33 and 0.68 respectively (Table 4). The strong unrealistic in-phase relation between ISMR and EIOD is significantly reduced in MMCFSv2 from 0.68 to 0.33.
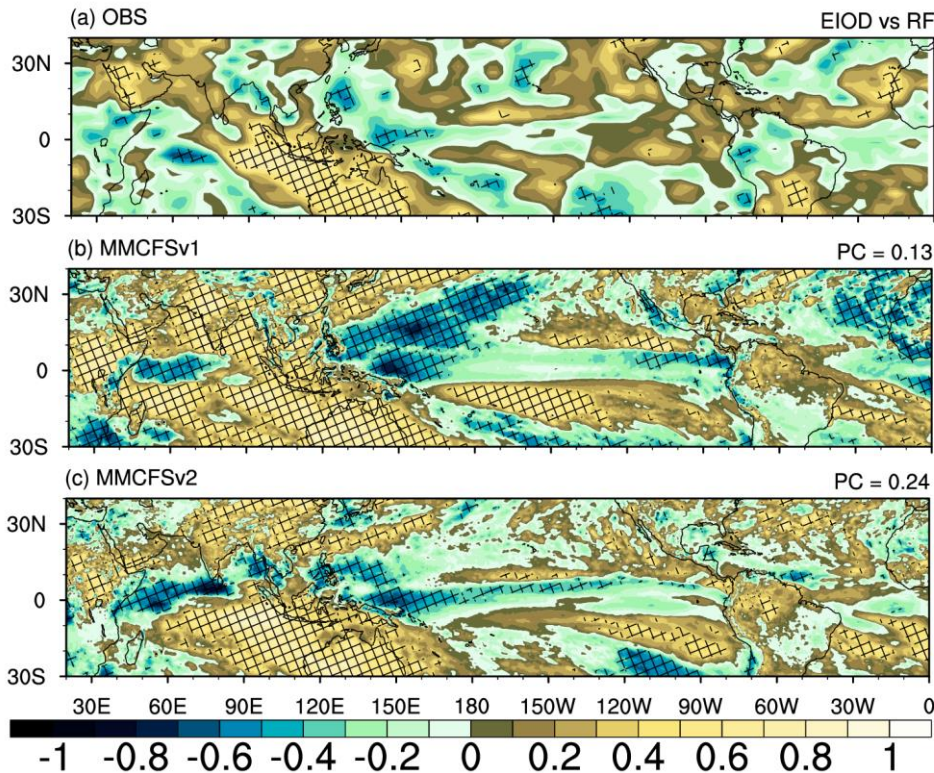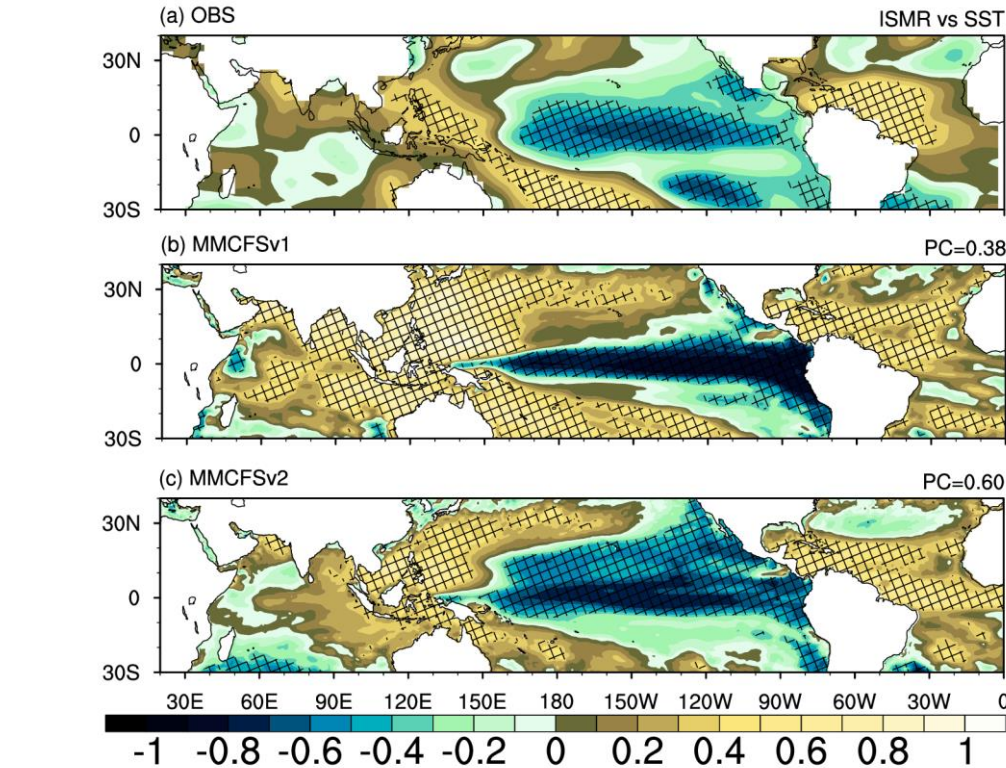

Figure 17: Correlation between the SST anomalies over the eastern equatorial Indian Ocean (index) and rainfall anomalies over the tropical regions. (a) Observations (GPCP), (b) MMCFSv1, and (c) MMCFSv2. The hatching shows statistical significance at 95 % confidence level.

Figure 18 shows the simultaneous correlation between the JJAS ISMR anomaly index and tropical SST anomalies. Observed ISMR correlates significantly (negatively) with SST anomalies over central-North Pacific (around 0-20° N, 150-240° E). The correlation is weaker and positive over the northwestern Pacific region. ISMR is significantly (positively) correlated with SST anomalies over the North Atlantic region and is weakly correlated with Indian Ocean SST anomalies

(observations in Fig. 18 (a)). Both models overestimate this correlation over the western north Pacific region compared to observations. MMCFSv1 shows stronger teleconnections between ISMR and Pacific Ocean compared to MMCFSv2 (stronger negatives over central and east Pacific, and stronger positives over west Pacific). Northern Atlantic SST anomalies are well captured by both models (Fig. 18 (b), (c)). MMCFSv2 can reproduce the observed correlation over the Indian and Pacific oceans much better than MMCFSv1. Overall, the pattern correlation between the MMCFSv2 and observed teleconnection is much higher (at 0.60) than MMCFSv1 (at 0.38). We further assessed the model in simulating the teleconnection between Atlantic meridional and zonal modes and ISMR and found that MMCFSv2 cannot simulate the observed AZM and AMM teleconnections (Table 4).

Figure 18: Correlation between ISMR and global SST anomalies. (a) Observations (ERSST), (b) MMCFSv1, (c) MMCFSv2. The hatching shows statistically significant at a 95% confidence level.

1. **Summary and Discussion**

25

A new Monsoon Mission Coupled Forecast System version 2 (MMCFSv2) model has been deployed at IITM to replace the currently operational MMCFSv1. MMCFSv2 brings in a substantial number of component upgrades over the MMCFSv1. These upgrades include the use of the MOM6 ocean model over MOM4. CICE5 model over SIS sea-ice model of MMCFSv1, Semi-Lagrangian dynamical core for integrating the GFS atmospheric model over the Eulerian one used previously. The coupler in the MMCFSv1 is based on the NEMS framework. This framework allows the model to interface with numerous external model components and brings in much-needed modularity for easy future upgradability. Coupled hindcast simulations with April initial conditions from CFSR have been carried out for 25 years (from 1998 to 2022). This dataset will be the baseline for future sensitivity studies using MMCFSv2.

We documented the MMCFSv2 model skill (compared to MMCFSv1) in simulating mean tropical SST, precipitation, and circulation. We also documented the skills in simulating Indian Summer Monsoon at seasonal time scales, mean and inter annual variability of ISMR and its teleconnections with ENSO and IOD, AMM, and AZM. MMCFSv2 captures all the large-scale features during the JJAS season reasonably well. It shows improvements in many large-scale meteorological features over MMCFSv1. The wet rainfall bias over the north Pacific is reduced considerably in MMCFSv2 compared to MMCFSv1. The wind shear bias is reduced considerably in MMCFSv2. Lower tropospheric winds are much better simulated in MMCFSv2 compared to MMCFSv1. One of the biggest weaknesses of most climate models in simulating the Indian monsoon is the dry bias compared to observations. MMCFSv2 reduced this bias compared to MMCFSv1. MMCFSv2 much better simulates upper and lower tropospheric winds. Wind shear is also much closer to observations over Indian landmass in MMCFSv2 compared to MMCFSv1.

MMCFSv2 showed improvements in reproducing mean of JJAS rainfall over MMCFSv1 by reducing the bias from 1.32 to 1.04 (~4 %) with respect to GPCP. MMCFSv2 captured the observed (GPCP) phase of interannual variability with a higher skill of 0.72 over 0.55 of MMCFSv1. Hence, MMCFSv2 improved the phase skill by 30 % and amplitude skill by about 20 %. MMCFSv2 reduced the NRMSE from 1.06 of MMCFSv1 to 0.82 with respect to GPCP, which is about 20%. Compared to the NMME models, MMCFSv2 has the highest skill in capturing the interannual variability of ISMR (ACC=0.72). MMCFSv2 SD is very close to observations (normalized SD = 0.96), and it has one of the least NRMSE values (0.82). Further, the MMCFSv2's actual skill is (0.72) is very close to the potential skill (0.79) and is a large improvement over MMCFSv1. MMCFSv2 has also attained the theoretical predictability limit of ~0.7. It was noticed that MMCFSv2 improves the simulated large-scale teleconnection pattern between Nino 3.4 index and tropical SST with a higher pattern correlation of 0.70 compared to 0.63 of MMCFSv1. The spatial pattern of correlation between ERSST over the eastern Indian ocean dipole (EIOD) box (10° S to the Equator, 90-110° E) and tropical SSTs anomalies has improved (pattern correlation of teleconnections from 0.31 in MMCFSv1 to 0.38 in MMCFSv2). MMCFSv2 did not reproduce the Nino3.4 induced SST patterns over the Atlantic Ocean, whereas it is well captured by MMCFSv1. MMCFSv2 captured the eastern Indian Ocean-induced SST pattern over the Tropical Oceans, which was weaker in MMCFSv1.

The simultaneous correlation between the JJAS ISMR anomaly index and tropical SST anomalies showed that both models overestimated the correlation over the western north Pacific region compared to observations. MMCFSv1 showed stronger teleconnections between ISMR and Pacific Ocean compared to MMCFSv2 (stronger negatives over central and east Pacific, and stronger positives over west Pacific). MMCFSv2 reproduced the observed correlation patterns with a higher pattern correlation of 0.60 compared to 0.38 of MMCFSv1. Overall, MMCFSv2 captured the teleconnection between ISMR and tropical SST anomalies closer to observations than MMCFSv1.

One of the potential research areas with coupled climate models in general and MMCFSv2 is the sea surface and air temperatures biases compared to observations. The increased surface temperatures in MMCFSv2 resulted in warmer tropospheric columns in the summer hemisphere. MMCFSv2, however, simulated temperatures closer to observations in the winter hemisphere. Given that the use of MOM6 over MOM4 has enabled us to use many more parameterizations, we will address this problem in a future study. The present study's focus was to present the climatological characteristics simulated by MMCFSv2.

To summarize, the mean state of the atmosphere has improved in MMCFSv2 (compared to MMCFSv1), both in terms of precipitation and circulation (850hPa winds). This has resulted in improved teleconnections (Figure 16). The pattern correlation between spatial structure of teleconnections in Figure 16 (manuscript) has improved from 0.38 in MMCFSv1 to 0.60 in MMCFSv2. Hence the interannual variability skill has improved. MMCFSv2 improves many meteorological fields compared with MMCFSv1 in ISMR hindcasts. However, the NEMS coupling framework is the biggest improvement MMCFSv2 brings over MMCFSv1. This is central to making it easier to upgrade the individual model components as and when their respective scientific groups improve them. This is very important for an operational model.

Code and Data availability

The current version of MMCFSv2 used for this study is available at https://doi.org/10.5281/zenodo.7905721 (Please check the license files for individual component model in the repository). The data used for the analysis in this manuscript is available at https://zenodo.org/record/7900790#.ZFU-T5FBxcA (DOI : 10.5281/zenodo.7900790). The complete (processed) data used to initialize and run the MMCFSv2 simulations from 1998-2022 is made available at

Input data from 1998 to 2000 - https://doi.org/10.5281/zenodo.7935628, from 2001 to 2003 - https://doi.org/10.5281/zenodo.7947318, from 2004 to 2006 - https://doi.org/10.5281/zenodo.7947974, from 2007 to 2009 - https://doi.org/10.5281/zenodo.7948155, from 2010 to 2012 - https://doi.org/10.5281/zenodo.7949802, from 2013 to 2015 - https://doi.org/10.5281/zenodo.7950855, from 2016-2018 - https://doi.org/10.5281/zenodo.7949863, from 2019-2021 - https://doi.org/10.5281/zenodo.7950964, and for 2022 - https://doi.org/10.5281/zenodo.7951983

Please note that the original raw data belongs to NCEP (Saha, Suranjana, and Coauthors, 2010: The NCEP Climate Forecast System Reanalysis. Bull. Amer. Meteor. Soc., 91, 1015, S1057. https://doi.org/10.1175/2010BAMS3001.1).

Competing Interests

The authors have no relevant financial or non-financial interests to disclose.

Authors' contributions

The study was conceptualized by Suryachandra A. Rao. The model deployment and simulations were carried out by Deepeshkumar Jain. The analysis was performed by Deepeshkumar Jain and Ramu A. Dandi. Ankur Srivastava and Maheswar Pradhan helped in MMCFSv1 simulations. Prasanth A. Pillai

helped in NMME data analysis. Kiran VG carried out the heat budget analysis of MMCFSv2 ocean model. The first draft of the manuscript was written by Deepeshkumar Jain and all authors commented on previous versions of the manuscript. All authors read and approved the final manuscript.

Availability of data and materials

585 The data used for analysis in this manuscript is available at https://zenodo.org/record/7900790#.ZFU-T5FBxcA (DOI : 10.5281/zenodo.7900790). The documentation for CICE5 is available at https://cice-consortium-cice.readthedocs.io/en/cice6.0.0.alpha/index.html .

Disclaimer

590 Publisher's note: Copernicus Publications remains neutral with regard to jurisdictional claims in published maps and institutional affiliations. The views expressed in this document are solely those of the authors.

Financial Support

595 The authors declare that no funds, grants, or other financial support were received during the preparation of this manuscript.

Acknowledgements

References

1. Adcroft, A. (2016) Modular Ocean model (mom), https://www.gfdl.noaa.gov/mom-ocean-model/

2. Adler, R.F., Huffman, G.J., Chang, A., Ferraro, R., Xie, P.P., Janowiak, J., Rudolf, B., Schneider, U., Curtis, S., Bolvin, D. and Gruber, A., The version-2 global precipitation climatology project (GPCP) monthly precipitation analysis (1979–present). *Journal of hydrometeorology*, *4*(6), pp.1147-1167, DOI: https://doi.org/10.1175/1525-7541(2003)004<1147:TVGPCP>2.0.CO;2, 2003.

3. Ahmadabadi, A., et al. "The accuracy of SST retrievals from NOAA-AVHRR in the Persian Gulf." *Journal of Applied Sciences* 9.7: 1378-1382, 2009

4. Ashok, K., Guan, Z., Saji, N.H. and Yamagata, T., Individual and combined influences of ENSO and the Indian Ocean dipole on the Indian summer monsoon. *Journal of Climate*, *17*(16), pp.3141-3155, DOI: https://doi.org/10.1175/1520-0442(2004)017<3141:IACIOE>2.0.CO;2, 2004.

5. *Balaji, V., FMS: the GFDL Flexible Modeling System. Princeton, NJ, 67, 2004.*

6. *Benke, Mahendra, et al. "Analysis of Monsoon Mission Coupled Forecasting System (MMCFS) model simulations of sub-division scale temperatures over India for the hot weather season (April–June)." Journal of Earth System Science 128: 1-22, 2019*

7. Iredell, M., Black, T. and Lapenta, W., The NOAA Environmental Modeling System at NCEP. In *26th Conf. on Weather Analysis and Forecasting/22nd Conf. on Numerical Weather Prediction,* 2014.

8. Chaudhari, H.S., Pokhrel, S., Saha, S.K., Dhakate, A., Yadav, R.K., Salunke, K., Mahapatra, S., Sabeerali, C.T. and Rao, S.A., Model biases in long coupled runs of NCEP CFS in the context of Indian summer monsoon. *International Journal of Climatology*, *33*(5), pp.1057-1069, DOI: https://doi.org/10.1002/joc.3489, 2013.

9. Choudhury, B.A., Rajesh, P.V., Zahan, Y. and Goswami, B.N., Evolution of the Indian summer monsoon rainfall simulations from CMIP3 to CMIP6 models. *Climate Dynamics*, pp.1-26, DOI: 10.1007/s00382-021-06023-0, 2021.

10. CICE, R.C., Bailey, D., DuVivier, A., Holland, M., Hunke, E., Lipscomb, B., Briegleb, B., Bitz, C. and Schramm, J., CESM CICE5 Users Guide, 2018.

11. Craig, A., Valcke, S. and Coquart, L., Development and performance of a new version of the OASIS coupler, OASIS3-MCT_3. 0. *Geoscientific Model Development*, *10*(9), pp.3297-3308, DOI: https://doi.org/10.5194/gmd-10-3297-2017, 2017.

12. Delworth, T.L., Broccoli, A.J., Rosati, A., Stouffer, R.J., Balaji, V., Beesley, J.A., Cooke, W.F., Dixon, K.W., Dunne, J., Dunne, K.A. and Durachta, J.W., GFDL's CM2 global coupled climate models. Part I: Formulation and simulation characteristics. *Journal of Climate*, *19*(5), pp.643-674, DOI: https://doi.org/10.1175/JCLI3629.1, 2006.

13. Ding, Hui, Noel S. Keenlyside, and Mojib Latif. "Equatorial Atlantic interannual variability: Role of heat content." *Journal of Geophysical Research: Oceans* 115.C9, DOI: 10.1029/2010JC006304

14. (2010).

15. Ek, M.B., Mitchell, K.E., Lin, Y., Rogers, E., Grunmann, P., Koren, V., Gayno, G. and Tarpley, J.D., Implementation of Noah land surface model advances in the National Centers for Environmental Prediction operational mesoscale Eta model. *Journal of Geophysical Research: Atmospheres*, *108*(D22), DOI: https://doi.org/10.1029/2002JD003296, 2003.

640

16. Fan, X., Duan, Q., Shen, C., Wu, Y. and Xing, C., Global surface air temperatures in CMIP6: historical performance and future changes. *Environmental Research Letters*, *15*(10), p.104056, DOI: https://doi.org/10.1088/1748-9326/abb051, 2020.

17. Farneti, R., Stiz, A. and Ssebandeke, J.B., Improvements and persistent biases in the southeast tropical Atlantic in CMIP models. *npj Climate and Atmospheric Science*, *5*(1), p.42, DOI: https://doi.org/10.1038/s41612-022-00264-4,

645

18. Findlater, J., A major low-level air current near the Indian ocean during the northern summer. Quarterly Journal of the Royal Meteorological Society **95**(404), 362–380, DOI: https://doi.org/10.1002/qj.49709540409, 1969.

19. Gadgil, S., The Indian monsoon and its variability, Annual Review of Earth and Planetary Sciences **31**(1), 429–467, DOI: https://doi.org/10.1146/annurev.earth.31.100901.141251, 2003.

650

20. Gadgil, S., The Indian monsoon, GDP and agriculture. Economic and political weekly, 4887–4895, DOI: https://doi.org/10.2307/4418949, 2006.

21. George, G., Rao, D.N., Sabeerali, C., Srivastava, A., Rao, S.A. Indian summer monsoon prediction and simulation in cfsv2 coupled model. Atmospheric Science Letters **17**(1), 57–64, DOI: https://doi.org/10.1002/asl.599, 2016.

22. Goswami, B.B., Deshpande, M., Mukhopadhyay, P., Saha, S.K., Rao, S.A., Murthugudde, R., Goswami, B.,

655

Simulation of monsoon intraseasonal variability in ncep cfsv2 and its role on systematic bias. Climate dynamics **43**(9), 2725–2745, DOI: https://doi.org/10.1007/s00382-014-2089-5, 2014.

23. Griffies, S.M., Harrison, M.J., Pacanowski, R.C., Rosati, A., A technical guide to mom4. GFDL Ocean Group Tech. Rep **5**, 342, 2004.

24. Hersbach, H., B. Bell, P. Berrisford, S. Hirahara, A. Horányi, J. Muñoz-Sabater, and A. Simmons., The era5 global

660

reanalysis. Quarterly Journal of the Royal Meteorological Society **146**(730), 1999–2049, 2020.

25. Hill C, DeLuca C, Suarez M, Da Silva AR. The architecture of the earth system modeling framework. Computing in Science & Engineering; 6(1):18-28, DOI: https://doi.org/10.1109/MCISE.2004.1255817, 2004.

26. Huang, B., Thorne, P.W., Banzon, V.F., Boyer, T., Chepurin, G., Lawrimore, J.H., Menne, M.J., Smith, T.M., Vose, R.S., Zhang, H.-M., Extended reconstructed sea surface temperature, version 5 (ersstv5): upgrades, validations, and

665

intercomparisons. Journal of Climate **30**(20), 8179–8205, DOI: https://doi.org/10.1175/JCLI-D-16-0836.1, 2017.

27. Huang, B., Angel, W., Boyer, T., Cheng, L., Chepurin, G., Freeman, E., Liu, C., Zhang, H.-M., Evaluating SST analyses with independent ocean profile observations. Journal of Climate **31**(13), 5015–5030, DOI: https://doi.org/10.1175/JCLI-D-17-0824.1, 2018.

28. Huang, B., Liu, C., Ren, G., Zhang, H.-M., Zhang, L., The role of buoy and Argo observations in two SST analyses in the global and tropical pacific oceans. Journal of Climate **32**(9), 2517–2535, DOI: https://doi.org/10.1175/JCLI-D-18-0368.1, 2019.

29. Huang, B., Menne, M.J., Boyer, T., Freeman, E., Gleason, B.E., Lawrimore, J.H., Liu, C., Rennie, J.J., Schreck, C.J., Sun, F. and Vose, R., Uncertainty estimates for sea surface temperature and land surface air temperature in NOAA GlobalTemp version 5. *Journal of Climate*, *33*(4), pp.1351-1379, DOI: https://doi.org/10.1175/JCLI-D-19-0395.1, 2020

30. Huffman, G.J., Adler, R.F., Rudolf, B., Schneider, U., Keehn, P.R., Global precipitation estimates based on a technique for combining satellite-based estimates, rain gauge analysis, and NWP model precipitation information. Journal of Climate **8**(5), 1284–1295, DOI: https://doi.org/10.1175/1520-0442(1995)008<1284:GPEBOA>2.0.CO;2, 1995

31. Hunke, E.C., Lipscomb, W.H., Turner, A.K., Jeffery, N., Elliott, S., CICE: The Los Alamos Sea ice model documentation and software user's's manual version 5.1. LA-CC-06-012; Los Alamos National Laboratory: Santa Fe, NM, USA **115,** 2015.

32. Jiang, X., Li, T., Wang, B., Structures and mechanisms of the northward propagating boreal summer intraseasonal oscillation. Journal of Climate **17**(5), 1022–1039, DOI: https://doi.org/10.1175/1520-0442(2004)017<1022:SAMOTN>2.0.CO;2, 2004

33. Joseph, P., Raman, P., Existence of low-level westerly jet stream over peninsular India during July. Mausam, **17**(3), 407–410, DOI: https://doi.org/10.54302/mausam.v17i3.5731, 1966.

34. Kothawale D.R., RM, Monthly, seasonal and annual rainfall time series for all-India, homogeneous regions and meteorological subdivisions. IITM Research Report RR-138, 2017.

35. Krishna, R., Rao, S.A., Srivastava, A., Kottu, H.P., Pradhan, M., Pil- lai, P., Dandi, R.A., Sabeerali, C., Impact of convective parameterization on the seasonal prediction skill of Indian summer monsoon. Climate Dynamics **53**(9), 6227–6243, DOI: https://doi.org/10.1007/s00382-019-04921-y, 2019.

36. Krishnamurti, T.N., Bhalme, H., Oscillations of a monsoon system. part i. observational aspects. Journal of Atmospheric Sciences **33**(10), 1937–1954, DOI: https://doi.org/10.1175/1520-0469(1976)033<1937:OOAMSP>2.0.CO;2, 1976.

37. Kumar, J.R., Dash, S., Inter-annual and intra-seasonal variation of some characteristics of monsoon disturbances formed over the bay. Mausam **50**(1), 55–62, DOI: https://doi.org/10.54302/mausam.v50i1.1804, 1999a.

38. Kumar, K.K., Rajagopalan, B., Cane, M.A., On the weakening relationship between the Indian monsoon and ENSO. Science **284**(5423), 2156–2159, DOI: https://doi.org/10.1126/science.284.5423.2156, 1999b.

39. Mohan, R.A., Goswami, B., A common spatial mode for intra-seasonal and inter-annual variation and predictability of the Indian summer monsoon. Current Science, 1106–1111, 2000.

40. Moorthi, S., H. L. Pan, and P. Caplan, Changes to the 2001 NCEP Operational MRF/AVN Global Analysis/Forecast System, Tech. Proced. Bull., Ser. No. 484, Natl. Weather Serv., Off. of Meteorol., 2001.

41. Mukhopadhyay, P., Prasad, V. S., Phani, R., Deshpande, M., Ganai, M., Tirkey, S., Sarkar, S., Performance of a very high-resolution global forecast system model (GFS T1534) at 12.5 km over the Indian region during the 2016–2017 monsoon seasons. *Journal of Earth System Science* 128: 1-18, DOI: https://doi.org/0.1007/s12040-019-1186-6, 2019

42. Munot, A., Kothawale, D., Intra-seasonal, inter-annual and decadal scale variability in summer monsoon rainfall over India. International Journal of Climatology: A Journal of the Royal Meteorological Society **20**(11), 1387–1400, DOI: https://doi.org/10.1002/1097-0088(200009)20:11<1387::AID-JOC540>3.0.CO;2-Z, 2000.

43. Pai, D. S., Rajeevan, M., Sreejith, O. P., Mukhopadhyay, B., Satbha., N. S., Development of a new high spatial resolution (0.25× 0.25) long period (1901-2010) daily gridded rainfall data set over India and its comparison with existing data sets over the region. *Mausam* 65, no. 1: 1-18., DOI: https://doi.org/10.54302/mausam.v65i1.851, 2014.

44. Parthasarathy, B., Kumar, K.R., Munot, A., Homogeneous Indian monsoon rainfall: variability and prediction. Proceedings of the Indian Academy of Sciences-Earth and Planetary Sciences **102**(1), 121–155, DOI: https://doi.org/10.1007/BF02839187, 1993.

45. Pillai, P.A., Rao, S.A., Ramu, D.A., Pradhan, M., George, G., Seasonal prediction skill of Indian summer monsoon rainfall in NMME models and monsoon mission cfsv2. International Journal of Climatology **38**, 847–861, DOI: https://doi.org/10.1002/joc.5413, 2018a.

46. Pillai, Prasanth A., Suryachandra A. Rao, Renu S. Das, Kiran Salunke, and Ashish Dhakate, Potential predictability and actual skill of Boreal Summer Tropical SST and Indian summer monsoon rainfall in CFSv2-T382: Role of initial SST and teleconnections. *Climate Dynamics* 51, no. 1: 493-510, DOI: https://doi.org/10.1007/s00382-017-3936-y, 2018b.

47. Pillai, P.A., Rao, S.A., Srivastava, A., Ramu, D., Pradhan, M., Das, R.S., Impact of the tropical pacific SST biases on the simulation and prediction of Indian summer monsoon rainfall in cfsv2, ECMWF system4, and NMME models. Climate Dynamics **56**(5), 1699–1715, DOI: https://doi.org/10.1007/s00382-020-05555-1, 2021.

48. Pillai, P.A., Rao, S.A., V. Gangadharan, K., Pradhan, M., Srivastava, A. and Jain, D.K., 2022. Impact of reduced ENSO variability and amplitude on ISMR prediction in the long-lead forecasts of monsoon mission CFS. *International Journal of Climatology*, *42*(16), pp.9166-9181., DOI: https://doi.org/10.1002/joc.7809, 2022.

49. Pokhrel, S., Rahaman, H., Parekh, A., Saha, S.K., Dhakate, A., Chaudhari, H.S., Gairola, R.M., Evaporation-precipitation variability over Indian ocean and its assessment in NCEP climate forecast system (cfsv2). Climate Dynamics **39**(9), 2585–2608, DOI: https://doi.org/10.1007/s00382-012-1542-6, 2012.

50. Pokhrel, S., Saha, S.K., Dhakate, A., Rahman, H., Chaudhari, H.S., Salunke, K., Hazra, A., Sujith, K. and Sikka, D.R., Seasonal prediction of Indian summer monsoon rainfall in NCEP CFSv2: forecast and predictability error. *Climate Dynamics*, *46*, pp.2305-2326., 2016.

735 51. Pradhan, M., Rao, S.A., Bhattacharya, A., Balasubramanian, S., Improvements in diurnal cycle and its impact on seasonal mean by incorporating COARE flux algorithm in CFS. Frontiers in Climate, 198, 2022.

52. Rajeevan, M., Bhate, J., Kale, J., Lal, B., High resolution daily gridded rainfall data for the Indian region: Analysis of break and active monsoon spells. Current science, 296–306, 2006.

53. Rajeevan, M., Francis, P., Monsoon variability Links to major oscillations over the equatorial pacific and Indian
740 oceans. Current Science **93**(2), 182–194, 2007a.

54. Rajeevan, M., Pai, D., On the El Nino-Indian monsoon predictive relationships. Geophysical Research Letters **34**(4), DOI: https://doi.org/10.1029/2006GL028916, 2007b.

55. Ramu, D.A., Sabeerali, C., Chattopadhyay, R., Rao, D.N., George, G., Dhakate, A., Salunke, K., Srivastava, A., Rao, S.A., Indian summer mon- soon rainfall simulation and prediction skill in the cfsv2 coupled model: Impact of
745 atmospheric horizontal resolution. Journal of Geophysical Research: Atmospheres **121**(5), 2205–2221, DOI: https://doi.org/10.1002/2015JD024629, 2016.

56. Rao, S.A., Luo, J.-J., Behera, S.K., Yamagata, T., Generation and termination of Indian ocean dipole events in 2003, 2006 and 2007. Climate Dynamics **33**(6), 751–767, DOI https://doi.org/10.1007/s00382-008-0498-z , 2009.

57. Rao, S.A., Goswami, B.N., Sahai, A.K., Rajagopal, E.N., Mukhopadhyay, P., Rajeevan, M., Nayak, S., Rathore, L.S.,
750 Shenoi, S.S.C., Ramesh, K.J. and Nanjundiah, R.S., Monsoon mission: a targeted activity to improve monsoon prediction across scales. *Bulletin of the American Meteorological Society*, *100*(12), pp.2509-2532, DOI: https://doi.org/10.1175/BAMS-D-17-0330.1 , 2019.

58. Sabeerali, C.T., Ramu Dandi, A., Dhakate, A., Salunke, K., Mahapatra, S. and Rao, S.A., Simulation of boreal summer intraseasonal oscillations in the latest CMIP5 coupled GCMs. *Journal of Geophysical Research:*
755 *Atmospheres*, *118*(10), pp.4401-4420, DOI: https://doi.org/10.1002/jgrd.50403 , 2013.

59. Sabeerali, C., Ajayamohan, R., Bangalath, H.K., Chen, N., Atlantic zonal mode: an emerging source of Indian summer monsoon variability in a warming world. Geophysical Research Letters **46**(8), 4460–4467, DOI: https://doi.org/10.1029/2019GL082379, 2019.

60. Saha, S., Moorthi, S., Pan, H.L., Wu, X., Wang, J., Nadiga, S., Tripp, P., Kistler, R., Woollen, J., Behringer, D. and
760 Liu, H., The NCEP climate forecast system reanalysis. *Bulletin of the American Meteorological Society*, *91*(8), pp.1015-1058, DOI: https://doi.org/10.1175/2010BAMS3001.1, 2010.

61. Saha, S.K., Pokhrel, S., Chaudhari, H.S., Dhakate, A., Shewale, S., Sabeerali, C., Salunke, K., Hazra, A., Mahapatra, S., Rao, A.S., Improved simulation of Indian summer monsoon in latest NCEP climate forecast system free run. International Journal of Climatology **34**(5), 1628–1641, DOI: https://doi.org/10.1002/joc.3791, 2014.

765 62. Saha, S., Shrinivas, M., Xingren W., Jiande W., Sudhir N., Patrick T., Behringer, D., The NCEP climate forecast system version 2. *Journal of climate* 27, no. 6: 2185-2208, DOI: https://doi.org/10.1175/JCLI-D-12-00823.1 ,2014.

63. Saji, N., Goswami, B.N., Vinayachandran, P., Yamagata, T., A dipole mode in the tropical Indian ocean. Nature **401**(6751), 360–363, DOI: https://doi.org/10.1038/43854, 1999.

64. Semtner Jr, AJ., A model for the thermodynamic growth of sea ice in numerical investigations of climate. Journal of Physical Oceanography, **6**(3), 379–389, DOI: https://doi.org/10.1175/1520-0485(1976)006 ,1976.

65. Singh, P., Vasudevan, V., Chowdary, J., Gnanaseelan, C., Subseasonal variations of Indian summer monsoon with special emphasis on drought and excess rainfall years. International Journal of Climatology **35**(4), 570– 582, DOI: https://doi.org/10.1002/joc.4004, 2015.

66. Srivastava, A., Rao, S.A., Pradhan, M., Pillai, P.A., Prasad, V., Gain of one-month lead time in seasonal prediction of Indian summer monsoon prediction: comparison of initialization strategies. Theoretical and Applied Climatology **143**(3), 1083–1096, DOI: https://doi.org/10.1007/s00704-020-03470-3 , 2021.

67. Staniforth, A, and Jean C., Semi-Lagrangian integration schemes for atmospheric models. Monthly weather review 119.9 : 2206-2223, DOI: https://doi.org/10.1175/1520-0493(1991)119, 1991.

68. Taylor, K E., Summarizing multiple aspects of model performance in a single diagram." Journal of Geophysical Research: Atmospheres 106. D7 : 7183-7192, DOI: https://doi.org/10.1029/2000JD900719 , 2001.

69. Webster, P.J., Yang, S., Monsoon and Enso: Selectively interactive systems. Quarterly Journal of the Royal Meteorological Society **118**(507), 877–926, DOI: https://doi.org/10.1002/qj.49711850705 , 1992

70. Winton, M., A reformulated three-layer sea ice model. Journal of atmospheric and oceanic technology **17**(4), 525–531, DOI: https://doi.org/10.1175/1520-0426(2000)017 , 2000.

71. Zebiak, Stephen E., Air–sea interaction in the equatorial Atlantic region." *Journal of Climate* 6.8: 1567-1586, https://doi.org/10.1175/1520-0442(1993)006<1567:AIITEA>2.0.CO;2 (1993)

72. Zheng, Y., Shinoda, T., Lin, J.-L., Kiladis, G.N., Sea surface temperature biases under the stratus cloud deck in the southeast Pacific Ocean in 19 IPCC ar4 coupled general circulation models. Journal of Climate **24**(15), 4139–4164, DOI: https://doi.org/10.1175/2011JCLI4172.1, 2011.